Published in final edited form as:
Space Sci Rev. 2017 October ; 212(1-2): 553–584. doi:10.1007/s11214-017-0358-4.

Michelson Interferometer for Global High-resolution Thermospheric Imaging (MIGHTI): Instrument Design and Calibration

Christoph R. Englert[1,*], **John M. Harlander**[2], **Charles M. Brown**[1], **Kenneth D. Marr**[1], **Ian J. Miller**[3], **J. Eloise Stump**[4], **Jed Hancock**[5], **James Q. Peterson**[5], **Jay Kumler**[6], **William H. Morrow**[7], **Thomas A. Mooney**[8], **Scott Ellis**[9], **Stephen B. Mende**[10], **Stewart E. Harris**[10], **Michael H. Stevens**[1], **Jonathan J. Makela**[11], **Brian J. Harding**[11], and **Thomas J. Immel**[10]

[1]Space Science Division, U.S. Naval Research Laboratory, Washington DC 20375

[2]Space Systems Research Corporation, Alexandria, VA 22314

[3]LightMachinery Inc., Nepean, ON K2E 7L2, Canada

[4]Orbital/ATK, Beltsville, MD 20705

[5]Space Dynamics Laboratory, Logan, UT 84341

[6]Jenoptik Optical Systems LLC, Jupiter, FL 33478

[7]Resonance Ltd., Barrie, ON L4N 9V9, Canada

[8]Materion Corporation, Westford, MA 01886

[9]Photon Engineering, Tucson, AZ 85711

[10]Space Sciences Laboratory, University of California-Berkeley, Berkeley, CA 94720

[11]Department of Electrical and Computer Engineering, University of Illinois at Urbana-Champaign, Urbana, IL 61801

Abstract

The Michelson Interferometer for Global High-resolution imaging of the Thermosphere and Ionosphere (MIGHTI) instrument was built for launch and operation on the NASA Ionospheric Connection Explorer (ICON) mission. The instrument was designed to measure thermospheric horizontal wind velocity profiles and thermospheric temperature in altitude regions between 90km and 300km, during day and night. For the wind measurements it uses two perpendicular fields of view pointed at the Earth's limb, observing the Doppler shift of the atomic oxygen red and green lines at 630.0nm and 557.7nm wavelength. The wavelength shift is measured using field-widened, temperature compensated Doppler Asymmetric Spatial Heterodyne (DASH) spectrometers, employing low order échelle gratings operating at two different orders for the different atmospheric lines. The temperature measurement is accomplished by a multichannel photometric measurement of the spectral shape of the molecular oxygen A-band around 762nm wavelength. For each field of view, the signals of the two oxygen lines and the A-band are detected on different

* christoph.englert@nrl.navy.mil, +001 202-767-5528.

regions of a single, cooled, frame transfer charge coupled device (CCD) detector. On-board calibration sources are used to periodically quantify thermal drifts, simultaneously with observing the atmosphere. The MIGHTI requirements, the resulting instrument design and the calibration are described.

Keywords

ICON Explorer mission; Thermopspheric wind; Thermospheric temperature; Limb sounding; Spatial Heterodyne Spectroscopy

1. Introduction

1.1. Instrument Concept

The Michelson Interferometer for Global High-resolution imaging of the Thermosphere and Ionosphere (MIGHTI) instrument was designed to provide thermospheric wind and temperature measurements for the Ionospheric Connection (ICON) Explorer mission. The wind velocity observation is based on the Doppler shift measurement of the forbidden atomic oxygen red and green lines at the wavelengths of 630.0nm ($O(^1D \rightarrow {}^3P)$) and 557.7nm ($O(^1S \rightarrow {}^1D)$) respectively, imaging the limb of the Earth between 90 and 300 kilometers tangent point altitude during day and night. Wind directions are determined by combining observations of two fields of view that are directed nominally at an azimuth angle of 45 degrees and 135 degrees from the spacecraft ram direction, each providing line of sight wind components. To measure the Doppler shift, MIGHTI uses the Doppler Asymmetric Spatial Heterodyne (DASH) technique [Englert et al. 2007], which is a modified version of Spatial Heterodyne Spectroscopy (SHS) [Harlander et al. 1992].

The temperature observation is based on the radiometric measurement of three narrow band regions within the temperature dependent molecular oxygen Atmospheric band (A-band, $O_2(b^1\Sigma \rightarrow X^3\Sigma\ (0,0))$ around the wavelength of 762nm. Two additional passbands on either side of the band are used to observe the background contribution while avoiding signal from the (1, 1) vibrational band. The A-band observations are performed utilizing the same optics and detector as the wind observations and cover an altitude region of about 90-140km. In the following we provide an overview of the instrument heritage and describe details of the sensor design that was chosen based on the mission science requirements and available resources. In addition, we present results from the pre-launch calibration measurements.

1.2 Heritage

Measuring thermospheric wind profiles from satellites using Doppler shift observations of atmospheric emission lines has a rich history. Measurements have been performed using either Fabry-Perot interferometers [e.g. Rees et al., 1982; Hays et al. 1993; Killeen et al. 2006], a stepped Michelson interferometer [Shepherd et al. 1993], or a microwave spectrometer [Wu et al. 2007]. The Doppler Asymmetric Spatial Heterodyne (DASH) technique can be considered a combination of a stepped Michelson interferometer and a spatial heterodyne spectrometer and it was selected for the ICON mission because (1) the interferometer has no moving parts; (2) it can be field widened and therefore has a large

interferometric thoughput; (3) it is capable of measuring multiple lines simultaneously, which allows the periodic observation of a calibration line to track instrument drifts without losing atmospheric data and; (4) the creation of linear interference fringes enables the design of a sensor that images the required range of tangent points on the limb while avoiding a scanning mirror.

The spaceflight heritage of the MIGHTI wind measurement approach is based on two previously flown instruments that demonstrated all of the MIGHTI technologies and the measurement approach. The interferometric Doppler shift measurement of the atomic oxygen red and green lines was demonstrated by the highly successful WINDII (Wind Imaging Interferometer) instrument on the Upper Atmospheric Research Satellite (UARS) [Shepherd et al. 1993, 2012]. A monolithic spatial heterodyne spectrometer was demonstrated in orbit by the SHIMMER (Spatial Heterodyne Imager for Mesospheric Radicals) instrument on the Space Test Program Satellite-1 (STPSat-1) [Englert et al. 2010a]. In addition, the DASH technique was demonstrated by measuring thermospheric F-region winds using the oxygen red line from the ground, including a direct comparison with a ground based Fabry-Perot instrument [Englert et al. 2010b; Harlander et al. 2010; Englert et al. 2012].

The atomic oxygen emission line interferograms measured by a Michelson interferometer also contain information on the atmospheric temperature in the fringe contrast [Shepherd et al. 1993], however, determining the fringe contrast requires an accurate knowledge of all background signal contributions. Minimizing all background contributions and characterizing any residual signal is a challenge, especially during the day, when the Earth's illuminated disk, which would be just outside of a thermospheric limb sensor's field of view, provides signal strengths that are many orders of magnitude larger than the thermospheric airglow signal. Given this challenge and the fact that there are still unresolved questions about previous temperature observations that are based on fringe contrast measurements [Lathuillière et al. 2002], the temperature measurements for MIGHTI will use a radiometric measurement of the molecular oxygen A-band spectral shape. Measuring thermospheric temperatures from low Earth orbit using the oxygen A-band also has a long history. The A-band is one of the brightest emissions in the visible and near infrared airglow and was first measured from an aircraft in 1962 [Noxon and Vallence Jones 1962] and from a sounding rocket in 1968 [Wallace and Hunten 1968]. The temperature measurement exploits the temperature dependent band shape, a technique that has been used with limb sounding data since the late 1980s [Mende et al. 1988]. Most recent examples include the Remote Atmospheric and Ionospheric Detection System (RAIDS) on the International Space Station (ISS) [Christensen et al. 2013] and the Optical Spectrograph and InfraRed Imaging System (OSIRIS) on the ODIN satellite [Sheese et al. 2010, 2011].

2 Driving Instrument Requirements

The MIGHTI instrument design was driven by the ICON science requirements and the available spacecraft accommodations. The ICON science requirements generally flow down to measurement requirements for each instrument. One fundamental measurement requirement for MIGHTI is to measure the horizontal wind speed and direction. Since a

Doppler shift measurement is sensitive only to the wind velocity component parallel to the viewing direction (line of sight), MIGHTI uses two perpendicular fields of view nominally pointing 45° and 135° in azimuth from the spacecraft velocity (MIGHTI A and MIGHTI B). This way, the two MIGHTI fields of view measure virtually the same atmospheric volume about 8 minutes apart, given the targeted ICON orbit altitude of 575km [Immel et al. 2016]. The combination of colocated measurements at the observation tangent point then allows for the determination of the horizontal wind speed and direction [Harding et al. 2016]. This technique has been used successfully by previous satellite-based wind sensors [e.g. Shepherd et al. 1993]. MIGHTI measurement requirements for a single field of view are given in Table 1 for wind and in Table 2 for temperature.

To translate the MIGHTI measurement requirements to instrument component requirements, an instrument performance model was developed that simulates all major elements of the instrument and uses representative atmospheric volume emission rates (VER) and expected viewing geometries for observations at noon and midnight local solar time. The brightnesses for the atomic oxygen red and green lines, shown in Figure 1, were determined based on low and mid-latitude WINDII observations taken in 1996 [Guiping Liu, personal communication], during the solar activity minimum between solar cycle 22 and 23. The average brightnesses for the oxygen A-band are shown in Figure 2. The noon values were determined using low and mid-latitude RAIDS observations taken in 2010 [Christensen et al. 2012], during the solar activity minimum between solar cycle 23 and 24. The average midnight brightnesses for the oxygen A-band were chosen to be consistently lower than the low and mid-latitude WINDII observations of 1992-1994 [Liu 2006], corresponding to the declining phase of solar cycle 22.

The driving instrument parameters and their associated requirements are listed in the first two columns of Table 3. The first four requirements in the table are determined by the design geometry of the optics and are met with minor variations resulting from alignments, slightly oversized optics, and manufacturing constraints. The other requirements were treated as minimal performance limits with the goal to exceed them to maximize the instrument capabilities. The last column of Table 3 lists the as-built instrument performance characteristics.

3 Optical Design

As mentioned above, MIGHTI requires two perpendicular fields of view to measure horizontal wind vector components. Thus, the MIGHTI instrument consists of two identical optical sensors, MIGHTI A (Ahead) and MIGHTI B (Behind), which view the Earth's limb with perpendicular FOVs as shown in Figure 3(A). Figure 3(B) shows the optical sensors and the calibration lamp assembly prior to the integration onto the payload interface plate.

In addition to the optical sensors, MIGHTI consists of an external camera electronics assembly and an external calibration lamp assembly. The following sections provide details on the design of the main MIGHTI instrument components.

3.1 Baffle

Each MIGHTI sensor is equipped with a blackened baffle tube (see Figure 5) that extends forward of the entrance pupil located at A1. The primary purpose of the MIGHTI baffle is the suppression of signal that originates from angles outside the field of view. This is of vital importance, since the illuminated Earth's disk and the sun represent light sources that are many orders of magnitude brighter than the targeted airglow emissions, and during the day, the bright Earth is always close to the MIGHTI fields of view. Due to the ICON orbit and MIGHTI limb pointing geometry, the sun can also get close to or even enter the MIGHTI fields of view during the mission. A secondary purpose of the baffle is to reduce contamination from particles that could reach the first optical element and create a scattering source.

The design of the MIGHTI baffles adapted several features of the WINDII baffle [Gault et al. 1992], such as a two stage construction and the variable baffle exit aperture, A1. By design, the field stop and Lyot stop of the input optics (see Figure 6) limit the MIGHTI field of view (FOV) so that all of the baffle elements are outside the FOV. Light from outside the FOV can only enter the optical system by reflection off of baffle structures and then onto an optical surface. From there, it must be redirected into the FOV by scattering from the optical glass itself or from particulate contamination.

All inside surfaces of the baffle assembly were blackened with black Cytec BR 127NC ESD (electrostatic discharge) conductive epoxy primer. In addition to having low reflectivity, it is durable, cleanable, and able to withstand the temperatures in the MIGHTI survival specification. It has space flight heritage [Cheung et al. 2011] and in addition to blackening, it provides for increased adhesion of the epoxy used to glue the internal baffle vanes in place.

The overall baffle assemblies for MIGHTI A and B are 622mm long, limited by the envelope of the launch vehicle fairing. The baffles are designed as two stages according to principles described in Smith [1990]. The first stage lies in the 210mm of the assembly nearest A1. It is designed such that A1 can only see its exit window (AA) or the backside of an intervening baffle vane, as shown in Figure 7.

All incident light falls either on a sidewall of the baffle or the front of a baffle vane. The second stage begins at AA and extends to window AB at 622mm from A1. It also is designed so that AA can only see the backsides of vanes or the aperture AB. Since the sun can appear in the forward quadrant of the MIGHTI FOV, two additional baffle vanes are located just behind AB to increase the number of reflections needed by sunlight to reach AA and A1. Baffle vanes are made from rectangular aluminum sheets with rectangular cutouts. Each cutout has 30° knife edges that taper to a 0.05mm nominal edge. They have a coating of the BR 127 between 0.01mm and 0.025mm thick, so the knife edges were actually rounded with a small radius. It is worth repeating that all knife edges are outside the nominal FOV.

The AB aperture at the end of the baffle assembly is beyond the rest of the spacecraft and no S/C components, e.g. solar panels, are within a field of regard that is ±45° of the AB openings.

The detailed optical properties of BR-127 paint are not well documented in the literature and we have not endeavored to measure them. Visually, it appears to be approximately as black as Chemglaze Z306, but with a smoother surface texture. For our performance analysis below, we used 94% surface absorption, versus the 96% of Z306. Likewise, we have assumed a Lambertian scattering profile, but have avoided glancing reflections where the Lambertian assumption might fail. BR-127 was chosen despite the lack of detailed optical characterization data because it eliminated the requirement to coat the inside baffle surfaces after assembly and the application of epoxy to secure the baffle vanes, it optimized the sharpness of the vane edges since no additional coating had to be applied, it provided a surface that can dissipate static charges, it is durable and cleanable, and meets all thermal requirements.

Similar to the WINDII baffle, the MIGHTI baffles also include an exit aperture (A1) that can be changed in size to optimize the performance during the day when the Earth's disk is illuminated by the sun. A1 can be truncated from the top side in Figure 7 by a blackened, motor driven vane, so that in the "day" position only 15% of the aperture remains open and the rectangular aperture changes from a size of 30.78mm × 30.78mm to 30.78mm × 4.62mm. With the ability to truncate A1, the lowest tangent point altitude from which light can directly illuminate the first optical element after A1 during the day is 66km, which is well above the illuminated cloud tops on the limb. A1 can also be closed completely to perform dark measurements on orbit.

A detailed analysis of the baffle performance under these assumptions was conducted for the red line, green line and A-band emissions [Ellis 2015]. It includes stray light scattered from the baffle surfaces, scattering from contamination at a level of CL 400 on the optical surfaces, the optical surfaces themselves, and ghosting from the lenses. The cleanliness level CL 400 specifies the particle number and size distribution per surface area according to standard IEST-STD-CC1246D [Borson, 2004], with 400μm being the largest particle size in the distribution. This distribution function is commonly used for instruments that use contamination controls such as those implemented throughout the ICON program. The scattering is computed using a rigorous application of Mie scatter theory for spherical particles.

The goal was to achieve a stray light level of less than 10% (+25% margin, see Table 3) of the average daytime oxygen red line emission signal peak at 630nm (see Figure 1). The baffle performance specification was based on the red line signal which is the driving requirement since the green line signal and the A-band are generally brighter for the altitudes and times of the required MIGHTI measurements. Primary stray light sources are the bright Earth that lies below the FOV and the sun whenever it is in the forward quadrant. Models for these scenes were constructed together with a model of the baffle and of the MIGHTI entrance optics. The limb and disk radiance was modeled consistent with OSIRIS

measurements [McLinden et al. 2002]. Rays were traced to an image formed at the face of the MIGHTI gratings using the above assumptions.

Figure 8 shows results of the modeled scattered light performance for the oxygen red line when considering the illuminated Earth's disk. Panels (A) and (B) show the total flux on an idealized focal plane at the equivalent location of the MIGHTI interferometer gratings, where the limb scene is imaged. The model resulted in a total scattered and ghost light integrated flux of 1.2% compared to the total signal from the day time red line airglow within the FOV, illustrating that the performance goal of <10% of the maximum red line signal was met.

A second analysis was performed investigating the scattered light signal from the sun as the source, rather than the illuminated Earth. Using the ASTM E-490 AM0 specification for the extra atmospheric solar irradiance [ASTM 2000], Figure 9 shows the solar flux at the same image plane as in Figure 8. The analysis predicts that the above mentioned 10% relative flux goal is met at sun angles greater than 6° from the FOV.

3.2 Entrance optics

The MIGHTI entrance optics are shown in Figure 10 and include all optical elements between the first fold mirror (M1) and the interference filter (F1), located immediately in front of the interferometer. The purpose of the entrance optics is to (1) direct the beam from the baffle aperture (A1) onto the MIGHTI optical bench, (2) define the field of view for day and night aperture positions (note that the FOV is not defined by any baffle vanes), (3) superimpose signal from the calibration lamps onto the atmospheric signal, (4) eliminate signal from unwanted spectral regions between about 200-525nm and 900-1100nm, and (5) form an image of the limb at the fringe localization plane close to the gratings within the interferometer.

As shown in Figure 10, two flat mirrors (M1 and M2) are used to direct the beam onto the optical bench. The following lens, L1, simultaneously forms an image of the limb on the field stop and collimates light from the entrance pupil (A1). In front of the field stop is a cubic beam sampler which transmits 95% of the atmospheric signal and reflects into the beam 5% of the signal from the on-board calibration sources (see Section 4). Lens L2 collimates light from the field stop and images A1 onto the Lyot stop. The Lyot stop is slightly undersized with respect to the image of A1, so that the edges of A1 are blocked and the field of view is determined solely by the field stop and the Lyot stop. Immediately in front of the Lyot stop is a second adjustable aperture (A2). This aperture is equivalent to the adjustable aperture A1. In day mode, it also blocks about 85% of the rectangular Lyot stop by rotating a blackened vane into the beam. The vane is aligned so it blocks light originating from the edge of the daytime A1 aperture. Lens L3 collimates light from the Lyot stop and forms an image of the limb onto the fringe localization plane in the interferometer. The beam entering the interferometer is telecentric. The beam enters the interferometer enclosure after reflecting off a fold mirror (M3) and passing through a broad-band interference filter with a 525-900nm passband. This filter reduces light going into the interferometer that is within the sensitivity range of the MIGHTI CCD detector, but outside any wavelengths of interest.

The optical bench and M1 enclosure are thermally stabilized using three separate zones comprised of strip heaters, temperature sensors and PID (Proportional-Integral-Derivative) controllers. The bench is thermally controlled to maintain a temperature of about 20°C on orbit.

3.3 Interferometer

The DASH interferometer can be considered a combination of a stepped Michelson interferometer and a spatial heterodyne spectrometer. It consists of a beamsplitter and two interferometer arms of different lengths that are terminated with fixed, tilted diffraction gratings. Every individual groove of the grating is fundamentally equivalent to the return mirror in a stepped Michelson interferometer, and the imaging of the tilted grating allows the simultaneous measurement of many different optical path differences, corresponding to the positions of the grooves with respect to the beamsplitter. In addition, the MIGHTI interferometer is field widened with two fixed prisms positioned between the beamsplitter and the grating in each interferometer arm. Simultaneously sampling an optical path difference interval, the DASH interferometer superimposes low frequency spatial fringes oriented perpendicular to the horizon onto the limb image of the oxygen red and green line signals. The fringe frequencies are wavelength dependent, and are used to detect the Doppler shift of the emission lines. However, a wind velocity of v=3m/s results in a relative frequency change of only 10^{-8}, or one part in one hundred million. Instead of measuring the fringe frequency directly, the fringe pattern is measured around an optical path difference where the modulated signal is most sensitive to wind speed, which is similar to the stepped Michelson technique used by WINDII. The MIGHTI optical path difference center is about 5 cm or about 8.5×10^4 times the wavelengths of the targeted emission lines, so that the fringe phase change caused by a wind velocity of v=3m/s is about $10^{-8}\times8.5\times10^4\times2\pi \approx$ 5mrad or about 1/1000 of a fringe. Details about the DASH technique, including how to choose the optimal path difference and the fundamentals of the phase retrieval and error propagation are discussed in a publication by Englert et al. [2007] and, specifically for MIGHTI, in a companion paper by Harlander et al. [2017] in this issue.

The MIGHTI interferometers were designed to simultaneously work for the oxygen red and green lines. In addition, the interferometer efficiently transmits the wavelengths around 762nm, so that the wind and temperature measurements are made using the same optics and detector. To accommodate all three wavelengths, a field-widened DASH design was implemented using low order échelle diffraction gratings. The gratings were designed to work in 8^{th} order for the green line, in 7^{th} order for the red line and in 6^{th} order for the oxygen A-band. Note that the A-band measurement does not rely on measuring interference fringes, since the band shape measurement is based on a radiometric, narrow band filter approach [Stevens et al. 2016]. Details on the interferometer design and performance are discussed in a companion paper by Harlander et al. [2016].

The interferometer is integrated into a thermally controlled enclosure which is kept about 5°C above the optical bench temperature by dedicated strip heaters that are controlled using a high resolution temperature sensor and a PID controller (see Section 6.6).

3.4 Exit optics

The exit optics are all the optical elements between the interferometer and the CCD detector, which is located immediately behind a mosaic filter, as shown in Figure 10. The purpose of the exit optics is to spatially separate the signal of the green line from the red and infrared components to form two separate images of the fringe localization plane on the CCD focal plane array. Lens L4 collimates the light from the fringe localization plane within the interferometer and forms an image of the Lyot stop on the dichroic mirror. The dichroic mirror is a wedge shaped element that introduces an angular separation between the red/IR and green beams. Its first surface reflects the red beam components (red line and A-band) and transmits the green line signal. Its second surface, which is slightly tilted with respect to the first, reflects the green line signal. The first surface is plane and acts as a simple mirror. The second surface has a weak cylindrical shape to correct for the astigmatism introduced into the green beam by the thickness of the dichroic wedge. Mirror M4 redirects the beams toward the CCD. Lens L5 forms two images of the limb/fringe scene, one green and one red, on the focal plane array. The imaging is accomplished by collimating the signal from the dichroic wedge, which is an image of the entrance pupil and the Lyot stop. Thus, the beam onto the CCD is telecentric. Telecentricity makes the recorded fringe phase less sensitive to temperature drifts of the optical bench, since the first order effect of a camera misalignment in the direction of the beam does not change the fringe spacing (i.e., focus shift is not coupled to image magnification).

A mosaic filter containing seven narrow band interference filters, as shown schematically in Figure 11, is located immediately in front of the CCD. Two filter elements provide narrow spectral filtering for the green and red line images, and the other five elements are for the determination of the A-band shape and the broad band near infrared (NIR) background signal. Three of the NIR channels are located within the spectral region of the A-band while two channels are at slightly shorter and slightly longer wavelengths. Key filter specifications are given in Table 4. The exit optics were designed such that the green signal, which is reflected from the back side of the dichroic wedge is entirely transmitted by the green filter of the mosaic before it forms an image of the fringe/limb scene on one side of the CCD immediately behind the filter. The red line signal and the A-band signal, both of which are reflected by the front side of the dichroic wedge, are transmitted on the other half of the mosaic filter. Since the vertical direction in Figure 11 corresponds to the tangent point altitudes on the limb (perpendicular to the horizon), the signal originating from tangent point altitudes between about 90km and 140km passes through the A-band filters, while the signal originating between about 150km and 300km is transmitted by the red line filter. Using this geometry, the wind and temperature measurements can be accomplished simultaneously for these two different altitude regions using only one detector array for each MIGHTI field of view. To ensure that the signal levels from the red, green and A-band signals are compatible with the dynamic range of the CCD, the A-band filter peak transmittances were deliberately lowered to about 45%. In addition, the in-band reflection of the A-band filters was minimized by an indium-tin-oxide (ITO) coating to minimize multiple reflections between the filters and the interferometer. The mosaic filter was assembled from individual filters using opaque epoxy resin to avoid cross contamination by angled rays that would otherwise pass through substrate boundaries between filters.

The MIGHTI entrance and exit optics components are made from fused silica, BK7G18, and n-SF6, all of which are radiation hard glasses that show little darkening when exposed to the on-orbit radiation environment [Fruit et al. 2002].

4 Calibration Lamps

As with every interferometer, thermal effects are a potential concern. For MIGHTI, there are two different effects that need to be considered and mitigated. The first one is that thermal distortions of the structural hardware, such as the optical bench or the interferometer holder, could result in a shift of the image on the CCD detector. A lateral shift of the fringe image on the CCD is equivalent to a fringe phase shift and would therefore be interpreted as a Doppler shift. To detect and quantify lateral image shifts, a periodic notch pattern that is inscribed on one of the interferometer gratings is used [Harlander et al. 2016]. Using this notch pattern, sub-pixel scale movements can be detected and corrected as demonstrated by Englert et al. [2010b].

The second effect is a phase change due to a change in the optical path difference in the interferometer which could be caused by a thermal change in index of refraction of the interferometer field widening prisms, the thermal expansion of the diffraction gratings, and/or stresses induced in the interferometer due the differences in the coefficient of thermal expansion of the interferometer elements. A proven approach to quantify interferometer thermal drifts is to measure the fringe drift of calibration lamp lines that are spectrally close to the atmospheric red and green line emissions [Thuillier et al. 1998; Englert et al. 2010b]. The measured calibration line phase drifts directly track the equivalent phase drifts of the atmospheric signal. Note that the thermal phase drift due to the drift in image location on the CCD is a function of the spatial frequency of the recorded fringe pattern, which can be significantly different for the atmospheric and calibration lines, whereas the phase drifts originating from the interferometer are a function of the wavelength of the emission lines, which is chosen to be virtually identical for the atmospheric and calibration lines. Therefore, both the grating notches and calibration lamp signals are needed to unambiguously quantify and correct for all thermal drifts in the data analysis.

The on-board calibration lamps at 630.48nm (neon) and 557.03nm (krypton) provide two spectrally narrow emission lines that are close in wavelength to the oxygen red and green lines respectively and are used on-orbit to track and quantify thermal drifts of the interferometer. Both of these lines have been used successfully in previous instruments such as WINDII and REDDI [Shepherd et al. 1993, Englert et al. 2012].

The MIGHTI calibration lamps are electrode free, radio frequency (RF) excited discharge lamps that are based on previous lamp designs for the NASA Gravity Probe B, Wind and Hubble missions [Burchman, et al., 1998, Ogilvie, et al., 1995, Morrow, et al. 1993]. The two lamps are housed in one enclosure (see Figure 3) and each lamp requires 4W of unregulated power. The lamp assembly is passively cooled via radiative coupling of the assembly walls to the environment. Signal from the bulbs is coupled into one fiber bundle per lamp via a focusing lens. The two fiber bundles each contain 60 individual, fused silica, 200μm core diameter fibers. These bundles lead to a crossover assembly, where half of each

fiber bundle is rerouted to each of the MIGHTI sensors (A and B). Each sensor then receives a fiber bundle containing 30 fibers guiding red and 30 fibers guiding green signal. These "bicolored" fiber bundles interface with the calibration optic assembly shown in Figure 4. This assembly includes a fold mirror, an off-axis parabolic mirror to collimate the signal out of the fiber, an interference filter with a bandpass from 540-650nm and a holographic diffuser. The filter rejects any lamp signal that would contaminate the NIR channels of MIGHTI when the calibration lamps are on. The holographic, fused silica diffuser spreads the signal over approximately 20° in angle, overfilling the atmospheric beam angles, and is located near the beam splitter cube in the entrance optics shown in Figure 7. This beam splitter superimposes 5% of the calibration lamp signal onto the atmospheric signal. A false color image taken with the MIGHTI A detector is shown in Figure 12. It shows the fringe patterns formed by the krypton and neon calibration lines and on the bottom right the locations of the five NIR filters.

5 CCD Camera

MIGHTI uses two actively cooled CCD cameras based on the e2v CCD42-80 back illuminated detector chip [e2v technologies, 2006]. The CCD features a multiband antireflection coating to maximize quantum efficiency and is cooled to −40°C or below to minimize dark current. The 2048 × 4096 pixel format sensor has a pixel pitch of 13.5μm and is used in frame transfer mode to avoid a mechanical shutter. Figure 13 shows a cut-away of the camera head design.

Each MIGHTI sensor uses an identical camera head. The two camera heads are controlled by a single camera electronics assembly shown in Figure 3.

The CCD is oriented so that the frame transfer direction is parallel to the limb, which minimizes the transfer of pixels with low signal, e.g., at the top of the airglow layer, through areas of high signal, e.g., the maximum of the path integrated airglow layer. The main, as-built performance specifications of the MIGHTI cameras are given in Table 5.

CCD cooling is achieved using a thermoelectric cooler (TEC). The excess heat from the hot side of the TEC is conducted to a double sided radiator via an ammonia filled heat pipe, as shown in Figure 4.

The camera heads are fitted with vacuum windows so they can be evacuated in the laboratory and cooled to −40°C. This feature allows flight like test conditions on the ground without placing the entire instrument into a vacuum chamber. In addition, the polarity of the TEC can be reversed to heat the CCD to remove condensed contaminants on its surface on-orbit, if necessary.

Laboratory measurements showed that the two MIGHTI flight CCDs show a measurable amount of persistence, i.e., increased dark current for pixels that were previously illuminated. A detailed investigation of the persistence at a CCD temperature of −40°C showed that (1) the persistence effect is not present in the dark current after the CCD is cooled from room temperature in darkness; (2) the maximum persistence, or dark current increase, achieved with preceding saturated exposures, is equivalent to about 47 DN (Digital

Number output of the analog digital converter) per 60 second exposure which, with a gain of about 1.65 DN per electron, is equivalent to about 1.3 electrons per second per binned pixel (16×2) for MIGHTI B and about 0.2 electrons per second per binned pixel for MIGHTI A; (3) after maximizing the persistence effect, this additional dark current decays by about a factor of two after approximately two hours of reading out dark images once every minute; (4) the persistence effect is cumulative, i.e. a dark image taken after one exposure with a non-saturated count rate (e.g. 30,000DN, with saturation occurring at 2^{16}DN) shows less persistence than a dark image taken after two of the same non-saturated exposures; (5) the difference in persistence between the two detectors is an inherent property of the individual CCDs, not the read out electronics, so that the root cause might be small differences in the manufacturing process that are, for example, dependent on the chip position on the wafer. In summary, the persistence effect in MIGHTI B, which is about 6 times higher than in MIGHTI A, is a small fraction of the expected signal levels. Moreover, dark current corrections using dark exposures taken twice per orbit will provide a partial elimination of this effect due to its long decay time, which is more than the time it takes to complete one orbit. Also, periodic dark exposures will serve as a continuous verification that the persistence effect is not changing on orbit. Changes with mission duration are not expected since persistence has been traced to a constant characteristic of the individual CCD, caused by electron trapping or charge diffusion [Barrick et al. 2012].

6 MIGHTI Calibration

Before atmospheric wind and temperature profiles can be retrieved from MIGHTI observations, the raw data, or Level 0 (L0) data, must be processed to produce calibrated data, or Level 1 (L1) data. The main objective of the L0 to L1 processing is to correct any instrumental effects, so that an identical signal at each tangent point height, or CCD row, will result in the same response at the corresponding CCD row. For the wind measurements, this specifically includes the fringe phase and fringe amplitude reported in the L1 data.

Note that neither the retrieved wind velocity profiles, which depend on the phase and amplitude profiles of the measured interferograms versus tangent point altitude, nor the retrieved temperature profiles, which depend on the relative brightness profiles as a function of filter channel and tangent point altitude, require an absolute radiometric calibration of the MIGHTI instrument sensors.

Table 6 lists the L0 to L1 calibration steps that will be performed on the MIGHTI raw data. The following sections provide details on the individual steps. Note that for the A-band measurements, no flatfield or relative spectral response correction is performed to get to Level 1 data. The reason for this is that the A-band Level 2 data processing includes a correction for a potential common center wavelength shift of the A-band filters. This correction can account for thermal drift effects of the filter passbands and it can only be performed together with the retrieval of the atmospheric temperature profile [Stevens et al. 2016]. Therefore it is not included in the L0 to L1 data processing.

6.1 Dark current and bias correction

The CCD dark current and digital read-out bias level correction is accomplished by subtracting a dark image taken at the same integration time and focal plane temperature. Due to the long decay time for the CCD persistence effect, the dark correction also corrects for part of the persistence signal. Dark images can be taken on orbit by closing aperture A1. Periodic dark measurements will be taken on orbit to track changes in the dark current. To reduce the effect of read noise from an individual dark exposure a number of dark images will be averaged before subtraction. Changes in average dark images are expected due to the exposure of the CCD to the on-orbit radiation environment, which generally causes an increase in dark current and the creation of so called warm or hot pixels that show significantly increased dark current.

6.2 Spike removal

Spikes, or a spurious signal increase in one or more adjacent pixels, are caused on orbit by high energy radiation interacting with the CCD pixels. In addition, the MIGHTI images will contain the signature of stars, which will cause curved lines across the image due to their apparent movement during the exposures, which are 30 seconds and 60 seconds for day and night observations, respectively. Spikes and star tracks can be identified using the fact that the airglow signal varies slowly with altitude when viewed on the limb and averaged over an exposure. Image regions that have been identified as contaminated by a star or a spike are replaced using interpolated information from neighboring, unaffected pixels. This technique has been successfully applied to SHIMMER data [Englert et al. 2010a]. Similar to the MIGHTI, SHIMMER also used a CCD detector and the data also consisted of altitude dependent interferograms produced by a Spatial Heterodyne spectrometer. While SHIMMER data did not contain star images, due the design of its telescope, it did contain spikes from cosmic rays. Some cosmic ray events also produced tracks through several pixels, depending on the incident angle on the CCD.

6.3 Pixel transfer pick-up correction

The MIGHTI detectors use the e2v 42-80 CCD in frame transfer mode, where one half of the 2k×4k pixel array is used as the imaging area and the other half is used as the storage area. The atmospheric signal is imaged onto the imaging area of the CCD and at the end of the exposure it is quickly transferred to the storage area of the CCD which is optically masked. This allows a new exposure to begin while the previous image is read out. However, the image area is not shuttered during image transfer and each pixel briefly samples the signal falling on every other pixel in the row as it transfers through that location. To account for this extra signal pick-up, we subtract from every pixel in a row the amount of signal equal to the total signal in that row multiplied by the ratio of the row shift time (307.5ms) to the integration time (30s and 60s for day and night respectively). This approach is adequate since the transfer time is on the order of 1% or less of the exposure time. The CCDs are oriented in such a way that the pixels are transferred in the direction parallel to the horizon so that signal from one altitude does not contaminate that of other altitudes during the frame transfer process.

Since the transfer pick-up does not result in any significant modulated signal to the image, this effect has no direct effect on the retrieved fringe phase or Doppler speed.

6.4 Flatfield Correction

Flatfielding of the MIGHTI images is performed for two main reasons. First, the inversion of the limb images requires that the instrument response is independent of the tangent point altitude, or pixel row. This requires a cross calibration of the relative responsivity of all horizontal rows of the CCD. Second, pixel to pixel response variations within one row can have an effect on the retrieved phase of the interferogram [Marr et al. 2012]. This also requires a cross calibration between pixels.

6.4.1 Flatfield Correction for Red and Green Line Observations—Flatfield correction for SHS and DASH instruments has been discussed in detail by Englert et al. [2006] and Marr et al. [2012], and we describe in the following how we apply these techniques to the MIGHTI measurements.

The measured monochromatic interferogram signal for perfectly straight fringes, i.e., fringes that are aligned with the vertical columns of the focal plane array, can be written as a function of pixel row and column, I(x,y) [Englert et al., 2006]:

$$I(x,y) = \underbrace{\int_0^\infty B(\kappa)\left(t_A^2(\kappa,x,y) + t_B^2(\kappa,x,y)\right)d\kappa}_{Non-Modulated\ \ Term} + \underbrace{\int_0^\infty 2B(\kappa)\varepsilon(\kappa,x,y)t_A(\kappa,x,y)t_B(\kappa,x,y)\cos[2\pi\kappa x + \Theta(\kappa,x,y)]d\kappa}_{Modulated\ \ Term} \quad (1)$$

In Eq. (1) $B(\kappa)$ is the fringe frequency dependent spectral density, $[t_A(\kappa, x, y)\ t_B(\kappa, x, y)]$ accounts for the spectral and spatial dependence of the signal transmission through the instrument optics via the two interferometer arms (A & B) as well as the quantum efficiency of the detector pixels, $\varepsilon(\kappa, x, y)$ is the fringe modulation efficiency, and $\Theta(\kappa,x,y)$ is a phase distortion term.

In the MIGHTI L0 to L1 data analysis, the modulated term in Eq. (1) is isolated using the spectral isolation technique described by Englert et al. [2007]. Note that this step not only removes the non-modulated component from the targeted emission line, but also removes contributions from other lines that are outside of the spectral isolation function. This way, one can isolate the modulated part of only the atmospheric emission line or only the calibration lamp line from the interferogram.

For the now isolated, modulated term of the targeted line, the purpose of flatfielding is to ensure that any pixel to pixel differences in $[\varepsilon(\kappa, x, y)\ t_A(\kappa,x,y)\ t_B(\kappa,x,y)]$ are corrected, so that the resulting instrument response is uniform or "flat". It is worth repeating that no

absolute radiometric calibration is required, but a relative flatfield is needed, equalizing the relative response across the focal plane arrays.

For MIGHTI, flatfielding is done in two steps. First is the correction of non-uniformities in $[t_A(\kappa,x,y)\ t_B(\kappa,x,y)] = R(\kappa,x,y)$, which is the signal responsivity of the sensors as a function of wavelength and pixel. This is discussed in the next paragraph. Second is the correction of non-uniformities in the fringe modulation efficiency $\varepsilon(\kappa,x,y)$, which is discussed in section 6.4.3.

In order to obtain the relative response across the CCD for all targeted wavelengths, a relative spectral response measurement was made for both day and night configurations (A1=A2=15% open and A1=A2=100% open). To perform this measurement, the MIGHTI instrument was installed in a vacuum chamber and equipped with all necessary thermal ground support equipment, so that flight like thermal conditions could be maintained. Both MIGHTI sensors were oriented to view an integrating sphere through a chamber window. The integrating sphere was placed at the output of a Fourier Transform Spectrometer (FTS), which was illuminated with the spectral continuum of a quartz-halogen light source. As the path difference of FTS was step scanned, the MIGHTI focal planes were used as the detector for the FTS. By synchronizing the FTS interferometer mirror steps with the MIGHTI exposures, interferograms were measured for every binned MIGHTI pixel, yielding the desired relative spectral response for every binned MIGHTI pixel with a spectral resolution of $\delta\sigma$=9.64cm^{-1} which corresponds to $\delta\lambda\approx$0.38nm at λ=630nm (full width half maximum of FTS instrumental line shape function) [Peterson et al. 2016]. Panels A and B of Figure 14 show sample responsivities for wavelengths close to the oxygen red and green line.

6.4.2 Flatfield Correction for A-Band Observations—The temperature measurement, which is based on the background corrected relative signal contributions within the in-band NIR channels, also requires the detailed knowledge of the relative spectral response at each tangent point altitude. As described by the companion paper of Stevens et al. [2016], the three in-band filter channels (Filter #2, 3 and 4) allow the L1 to L2 data processing algorithm to determine a common passband shift of the filters in addition to the atmospheric temperature. Such a filter passband shift could be caused by changes in the A-band filter temperature.

As shown in panel C of Figure 14 for the example of NIR Filter #2, the relative spectral responses of the five NIR filters were determined using the technique described in Section 6.4.1. above. For the temperature retrieval it is particularly important to know the relative spectral shape of the filter transmittance, which was measured for each binned pixel. Figure 15 shows five spectral transmittances for one CCD row, or tangent altitude, as measured using flight-like thermal conditions.

6.4.3 Fringe Modulation Efficiency Correction for Red and Green Line Observations—The term $\varepsilon(\kappa,x,y)$ in Eq. (1) accounts for the fringe modulation efficiency. Non-uniformities in the fringe modulation can, for example, be caused by variations in the grating surface or the field widening prisms. In addition to instrumental effects, the fringe amplitude as a function of optical path difference (CCD column) is determined by the line

width of the measured source [Englert et al. 2007]. If a monochromatic source with infinitesimal linewidth were used to determine the modulation efficiency, the line width induced change in modulation could be identified and preserved. However, the MIGHTI wind measurement is independent of how the modulation efficiency changes with optical path difference (or the row variable *x*). Rather it is important for the inversion algorithm (L1 to L2 processing) that the modulation efficiency is constant with respect to all tangent point observations (or the column variable *y*). Therefore, it is possible to perform the MIGHTI modulation efficiency correction based on a measurement of a line with finite line width.

To determine the MIGHTI modulation efficiency for every binned pixel with the integrating sphere that was used for the relative spectral response measurement, we illuminated it with either an external neon or krypton lamp. External lamps were used with the integrating sphere to ensure the scene was uniformly illuminated.

The modulated part of dark and responsivity corrected neon line fringe patterns is plotted in Figure 16 (A) for CCD rows near the top and bottom of the altitude range. These rows were chosen because they show a significant difference in modulation or fringe amplitude, and are therefore well suited for demonstrating the correction.

Figure 16 (B) shows the modulation efficiency of the two interferograms in (A). The modulation efficiency was calculated in two steps. First, the phase of the fringe was calculated as described by Englert et al. [2007] and subsequently the interferogram was divided by the cosine of the phase. Pixels for which this cosine term in the denominator is comparable to or smaller than the interferogram uncertainty have a large sensitivity to phase noise and generally appear as spikes in the efficiency curves. However, the high signal to noise ratio of the measurement and the smooth shape of the efficiency versus pixel number allows the replacement of the small number of spikes using information from neighboring pixels via a three pixel median filter. Figure 16 (C) shows the modulation efficiency corrected fringe patterns, which are the ratio of the fringes shown in Panel (A) and the efficiencies shown in (B). Thus, for the uniformly illuminated scene generated by the integrating sphere, the corrected fringe patterns have constant amplitude across the optical path difference interval and, more importantly, they have the same amplitude for each CCD row.

Other than the spectral responsivity discussed in Section 6.4.1., the modulation efficiency cannot be measured for the exact wavelengths of the oxygen red and green lines because no suitable line sources are available on the ground. However, the modulation efficiency is expected to be virtually identical for the airglow lines and the corresponding neon and krypton calibration lines, because for a sub-percent difference in wavelength, the differences in grating properties, and beam geometry within the interferometer are negligible. Thus, the modulation efficiency determined before launch for the neon and krypton lines on the ground will be used in the analysis of the red and green line fringes measured on orbit.

It is also worth pointing out that even though the airglow distribution in the atmosphere is known to exhibit significant structure at scales that are comparable to the width of the MIGHTI field of view (3.22° or ~140km horizontally on the limb), the illumination across

each pixel row (constant altitude) is expected to be nearly constant. This is a consequence of the signal averaging that occurs during the MIGHTI integration times (30 and 60 seconds) during which the field of view moves approximately 230km and 460km respectively, due to the orbital velocity of the spacecraft.

6.5 Phase Correction for Thermal Image Shift

As described above, the MIGHTI optical bench and the interferometer are thermally controlled. Specifically, the bench is required to be held within ±2K and the interferometer enclosure is required to be held within ±100mK on orbit. Two different effects have the potential to cause thermal drifts of the fringe phase measurement. They are discussed in this Section and the next.

Thermal distortion of the predominantly aluminum MIGHTI structure has the potential to shift the fringe image on the focal plane array, which produces an apparent phase shift of the fringes. To quantify and, if necessary, correct this possible effect, a periodic notch pattern inscribed on one of the gratings for each MIGHTI interferometer is measured with each fringe exposure. The correction method is similar to the one applied for the REDDI instrument [Englert et al. 2010b]. It is based on the sub-pixel accuracy determination of the location of the notch pattern, which is imaged on the detector array along with the fringes (see Figure 12). For the MIGHTI gratings, the notches were inscribed using an excimer laser which evaporated much of the gold coating of the grating at the positions of the notches [Harlander et al. 2016]. As a result, the grating is less efficient inside the notches and the surfaces inside the notches are slightly recessed due to the surface ablation. Thus, the signal measured on the CCD from regions inside the notches is less intense than that from between the notches, but still shows an interference pattern. This interference pattern is phase shifted with respect to the fringe pattern from the regular grating surface due to the additional offset in optical path difference within the notches. The notches in the interferometer gratings are 0.2mm wide and have a spacing of 0.5mm.

Figure 17 shows a least squares fit of the signal within a pixel row that contains the notch pattern. The fit contains two fringe patterns, one inside the notches and one between the notches. Both patterns are phase shifted and amplitude adjusted based on the fringe pattern immediately below the notches. Oversampling of the fringe patterns by a factor of 1000 allows sub-pixel accuracy. To assess the magnitude of the thermally induced image shift, a simulation of the expected on-orbit thermal changes was conducted in a thermal-vacuum chamber. For this test the MIGHTI supply voltage was changed periodically to simulate the day/night spacecraft voltage changes expected on orbit. Since the thermal control of the MIGHTI sensor components is accomplished using feedback loops with strip heaters and thermal sensors, the control loops are affected when a change in voltage affects the heat flux delivered to the optical bench and the interferometer enclosure. This orbit simulation is discussed in more detail in Section 6.6 in the context of the interferometer thermal drift.

Figure 18 shows the image shift observed during the simulation of the anticipated on-orbit thermal changes. It shows that the image shift during the orbit simulation is on the order of two thousandths (0.002) of a pixel, which corresponds to a speed of about 1.0m/s for the red line and 0.5m/s for the green line. Based on this analysis, no significant image shift is

expected for the on-orbit thermal environment, i.e., image shifts correspond to Doppler speeds of about 1m/s or less.

6.6 Phase Correction for Interferometer Thermal Drift

In addition to the thermal image drift, temperature changes of the interferometer can also cause phase drifts. This effect is due to the thermal dependence of the index of refraction of the interferometer glasses, the thermal expansion of the interferometer components and stresses within the monolithic interferometer caused by the difference in thermal expansion of the different components [Marr et al. 2012]. To minimize this effect for the MIGHTI sensors, the interferometer is mounted in a gold coated enclosure that is thermally stabilized about 5°C above the optical bench temperature and equipped with heaters and temperature sensors that thermally stabilize the interferometer using a PID controller. Interferometer phase drift will be monitored on orbit by superimposing calibration lamp signal from on-board neon and krypton lamps on the atmospheric signal for one orbit every ~24 hours. These drifts are expected to be highly periodic following the orbit day/night transitions, with slow seasonal changes due to the changing orbit beta angle throughout the mission. Thus, assessing this correction for one orbit every ~24 hours is expected to be adequate.

The technique of correcting the atmospheric data with the fringe drifts determined from the calibration lamp signals is identical to the method described by Englert et al. [2010b] and Marr et al. [2013].

To assess the expected on-orbit magnitude of this effect, the orbit simulation data set used for the thermal image drift assessment in Section 6.5 was analyzed. For this analysis, the spacecraft voltage to the MIGHTI sensors, including the voltage to the MIGHTI heaters, was cycled in a step fashion, simulating the expected bus voltage variations during the mission's day/night cycle. The bus voltage variation for the experiment is shown in the bottom panel of Figure 19. The on-orbit voltage variations are expected to be similar in magnitude, but much smoother in time, so that this simulation represents a worst case.

The top panel of Figure 19 shows the change of the mean fringe phase for two tangent altitudes, referenced to the first exposure. The data shows that for low tangent altitudes (row #80; blue) the response to the bus voltage changes is much smaller than for high tangent altitudes (row #25; black). This is most likely due to the locations of the enclosure heaters, which are closer to the side of the interferometer that corresponds to the higher tangent altitudes. The mean phase for both rows shows a small drift (5mrad/6.5hours), which is attributed to the fact that the sensor had not fully thermally equilibrated from changes immediately preceding the thermal experiments. The temperatures of the sensor baseplate and the interferometer enclosure are shown in Figure 20.

For orbit simulation, three consecutive "orbits" were simulated by changing the bus voltage periodically. To assess how well the phase change can be corrected by using data from a different orbit, the data from the second orbit was compared to the data of the third orbit. The differences are shown in inset A and B of Figure 19, showing that the difference is dominated by statistical errors in the phase retrieval rather than the systematic features from the voltage variation. The standard deviation of the corrected phase is about 2.4mrad for the

red line. For the green line, a similar analysis yielded a value of less than 2.7mrad [MIGHTI Flight Model Calibration Report, 2016]. A phase change of 2.4mrad for the red line and 2.7mrad for the green line corresponds to less than 1.5m/s in wind velocity (see also Section 6.8) and if left completely uncorrected, the most sensitive altitudes (rows) would show a line of sight wind speed error of less than 6m/s. The correction is expected to remove the systematic error to less than the statistical error originating from photon shot noise (see Figure 19).

6.7 Phase Distortion Correction

For an idealized instrument, the fringe phase for a monochromatic signal is a linear function of the pixel number in each CCD row (i.e. $\Theta(\kappa,x,y)=0$ in Eq. (1)). In addition, for MIGHTI's two dimensional detector array and imaging approach, the fringe phase would be identical along each column of the CCD, i.e., independent of tangent point altitude. In reality however, any non-flatness of interferometer surfaces, a small roll or tilt of the grating, or index inhomogeneities in the interferometer glasses can cause departures from this ideal phase surface, resulting in fringes that appear slightly tilted and/or distorted. Since only small areas of the interferometer contribute to the signal detected at each individual pixel, these phase distortions generally do not decrease the fringe contrast.

Moreover, the phase distortion is a constant characteristic of the individual interferometer, so it can be measured and corrected in data analysis [Englert et al. 2004].

Figure 21 shows phase distortion curves for the example of the MIGHTI A red line fringes at all sampled tangent altitudes or CCD rows. They represent the difference between (1) the measured phases using an external neon line source, and (2) a phase surface that is linear in pixel number for each row and independent of pixel column. The measured phases are obtained using a uniformly illuminated field of view as described in Section 6.4.3. The 58 curves are for 58 CCD rows and the systematic slope change for changing tangent point height indicates that there is a small change in fringe frequency. This can also be seen in Figure 12, which shows more than half a fringe more on the top of the FOV as compared with the bottom of the FOV for the red-line fringes.

6.8 Interferometer Optical Path Difference

To convert phase differences into Doppler velocity differences, the following equation applies [Englert et al. 2007]:

$$\delta\varphi = 4\pi \times \Delta d(\mathrm{x}) \times \sigma \times \left(\frac{v}{c}\right) \quad (2)$$

Where $\delta\phi$ is the phase change, $2\Delta d$ is the optical path difference, x is the pixel number, σ is the wavenumber of the detected emission line, c is the speed of light and v is the Doppler velocity. According to Eq. 2, the phase change is a linear function of the absolute optical path difference at any given pixel.

The absolute path difference as a function of pixel number is determined by measuring the path difference at the center of the path difference interval and combining it with the path difference change per pixel, which is tightly constrained by the high precision interferometer components. The center path difference is measured, rather than using the design value, because the path difference offset was adjusted during the interferometer assembly to optimize the field widening performance of the interferometers [Harlander et al. 2016]. Therefore, the center path differences for each interferometer are expected to be slightly different.

For this measurement, signal from a neon lamp was reflected from a spinning disk, similar to the set-up shown in Figure 5 of Englert et al. [2007]. The neon line measurements resulted in the center path differences for the oxygen red-line listed in Table 7. The values for the oxygen green line are based on the red line measurement and a wavelength correction using a high fidelity optical model of the interferometer. The results are within the expected design range.

The path difference change from binned pixel to binned pixel is shown in Table 8, based on the as built interferometer components and the measured image magnification on the CCD, which is determined from the observed notch spacing.

6.9 Zero Wind Calibration

In order to determine the absolute fringe phase that corresponds to no Doppler shift ("zero wind") for the red and green line, a ground based measurement of the two atomic oxygen lines would be ideal. However, due to the forbidden nature of the two oxygen transitions, the upper states are very long lived and as a result, no lamps are available that can deliver bright, spectrally isolated oxygen red and green lines. The main problem is that the excited atoms get quenched by collisions before the desired photon is emitted.

Since the zero wind phases cannot be measured on the ground using lamps, the ICON mission includes periodic zero wind calibration maneuvers in which one MIGHTI sensor is first pointed toward the ram and subsequently toward the wake to sample the same air volume on the limb with antiparallel FOVs. A separate zero wind maneuver will be performed for each MIGHTI sensor in day and night modes. Assuming that the thermospheric wind does not change during the course of this maneuver, which is about 10 minutes long, the zero wind phase can be determined. For the correct zero wind phase, the two line of sight wind profile measurements have the same magnitude, but the opposite sign. The zero wind phase calibration is performed in the MIGHTI Level 2 data analysis and described by Harding et al. [2016]. The zero wind calibration data can also be used to verify the pre-launch phase distortion measurements. MIGHTI zero wind maneuvers will be conducted about once a month.

6.10 Field of view determination

The angular size of the MIGHTI fields of view is approximately 5.6° in altitude (vertical) and 3.4° in azimuth (horizontal) with small differences between the sensors due to the individual optical alignment, resulting in a total dayside étendue of about $0.055 cm^2 sr$. The altitude dimension is sampled with 87 binned pixel rows for both colors (IR/red and green).

The horizontal dimension, parallel to the limb is sampled with about 450 binned pixels per color. As shown in Figure 12, a small area on the top of the field of view is taken up by the grating notches to allow the quantification of any residual image drifts on the detector array.

The exact alignment of the fields of view with respect to the alignment cubes (see Figure 4) was measured in the laboratory to about 15arcsec using a collimated light source. Additional measurements were performed before and after vibration testing to verify that no major angular shifts occurred. Minor settling was expected. Since the launch environment is likely to cause further, minor changes in the absolute alignment of the fields of view with respect to the startrackers of the spacecraft, an on-orbit alignment calibration is planned in the ICON early orbit commissioning phase. For this purpose, the spacecraft will use inertial pointing, so that the MIGHTI sensors will be able to image a star field. For these exposures, the MIGHTI images will not be binned to provide the best angular resolution. This final alignment measurement will then be used for the MIGHTI pointing and data analysis, including the removal of the spacecraft velocity component from the Doppler shift measurement.

7 MIGHTI Level 1 Data Product

The MIGHTI Level 1 data product for the A-band measurements includes:

1. Start and end time of exposure.
2. Dark, bias, and spike corrected intensity values for each binned pixel behind the five IR mosaic filter components, excluding pixels that are near the filter edges. About 60% of the horizontal width of the filters is going to be used to avoid edge effects.
3. Uncertainties for the intensity values.
4. Quality flags indicating lower signal to noise (e.g., when the spacecraft is within the South Atlantic Anomaly), or a lack of calibration data.

The MIGHTI Level 1 data product for the oxygen red and green line measurements includes:

1. Start and end time of exposure.
2. Line of sight fringe phases versus optical path difference and pixel row number.
3. Line of sight fringe amplitudes versus optical path difference and pixel row number.
4. Uncertainty of fringe phases.
5. Uncertainty of fringe amplitudes.
6. Quality flags indicating lower signal to noise (e.g., when the spacecraft is within the South Atlantic Anomaly) a lack of calibration data, or the proximity to the terminator, which can significantly degrade the assumption of spherical symmetry of the atmosphere in the Level 2 analysis (see Harding et al. 2016).

A description of the MIGHTI Level 2 products for wind and temperature are described in companion papers by Harding et al. [2016] and Stevens et al. [2016]. They also include the propagation of the anticipated Level 1 data uncertainties to the uncertainties in the derived geophysical parameters (wind and temperature).

8 Summary

The Michelson Interferometer for High-resolution Imaging of the Thermosphere (MIGHTI) instrument was built for launch and operation on the NASA Ionospheric Connection Explorer (ICON) mission. The instrument was designed to measure thermospheric horizontal wind velocity profiles and thermospheric temperature in various altitude regions between 90km and 300km, during day and night. For the wind measurements it uses two perpendicular fields of view pointed at the Earth's limb, observing the Doppler shift of the atomic oxygen red and green lines at 630.0nm and 557.7nm wavelength. The wavelength shift is measured using field-widened, temperature compensated Doppler Asymmetric Spatial Heterodyne (DASH) spectrometers, employing low order échelle gratings operating at two different orders for the different atmospheric lines. The temperature measurement is accomplished by a multichannel photometric measurement of the spectral shape of the molecular oxygen A-band around 762nm wavelength. For each field of view, the signals of the two oxygen lines and the A-band are detected on different regions of a single, cooled, frame transfer charge coupled device (CCD) detector. Narrow band spectral filtering is achieved using a seven-element interference filter mosaic located immediately in front of the detector focal plane. The instrument design was predominantly driven by the wind observation requirements and the performance was modeled using atmospheric brightnesses typical for low solar activity. A heritage baffle concept was used to suppress signal from outside the field of view, which, during the day, is several orders of magnitude brighter than the signal from within the field of view. In the first step of the data analysis, from Level 0 to Level 1 data, instrumental effects are being removed from the raw, uncalibrated data. First, dark, read-out bias, spike, and transfer pickup corrections are performed. Next, flatfield and fringe modulation efficiency corrections are performed for the fringe patterns. Periodic notch patterns on the interferometer gratings are used to track and quantify thermal instrument drifts that result in image shifts on the CCD. Laboratory measurements simulating the expected on-orbit thermal environment show that this effect has only a very small effect on the fringe phase. Pre-launch phase distortion correction measurements are used to correct the interferometer specific, altitude dependent fringe distortions. Finally, two on-board calibration lamps are used to track and quantify thermal interferometer drifts, simultaneously with the atmospheric observations. The calibration lamp measurements are planned to be conducted for one orbit per 24 hour day.

The design and test measurements performed with the MIGHTI flight sensors show that the instrument meets the performance requirements of the NASA ICON mission.

Acknowledgments

ICON is supported by NASA's Explorers Program through contracts NNG12FA45C and NNG12FA42I. We acknowledge helpful discussions and advice from Prof. Gordon Shepherd (York University). We acknowledge the dedication and tireless work of all engineers, technicians and administrative support on the MIGHTI and larger

ICON team, including Rebecca Baugh, Patrick Bell, Joel Cardon, Angel Cerrato, James Cook, John Dancheck, Tori Fae, Tracy Heard, Steve Hershner, Lynn Hutting, Steve Kinaman, Will Marchant, Sally McCann, Miles Newman, David Nolan, John Pindell, Mark Ponton, Roger Prokic, Jack Sanders, John Shaw, Pedro Sevilla, Linda Smith, Tabetha Sykes, Steven Tanner, Warren Tolson, Emory Toomey, Drew Uhl, Mike Watson, Glenn Weigle, Vaz Zastera, and Dallas Zurcher.

References

ASTM 2000 Standard Extraterrestrial Spectrum Reference E-490-00 National Renewable Energy Laboratory; 2000 http://rredc.nrel.gov/solar/spectra/am0/ASTM2000.html. Accessed 17 June 2016

Barrick GA, Ward J, Cuillandre JC. Proc of SPIE. 2012; doi: 10.1117/12.926409

Cheung W, , Borowski HM, , Troll JR, , Wienhold PD. Development of solar Array substrates for the RBSP Spacecraft Society for the Advancement of Material and Process Engineering Conference; Spring. 2011 http://rbspgway.jhuapl.edu/sites/default/files/webform /dropbox/SAMPE_Spring_2011_RBSP_Solar_Array_Substrates_final.pdf, Accessed 13 May 2016

Buchman S, Bencze W, Brumley R, Keiser B, Clarke GM. The American Institute of Physics 1-56396-848-7/98, 178-187. 1998

Christensen AB, Bishop RL, Budzien SA, Hecht JH, Mlynczak MG, Russell JM III, Stephan AW, Walterscheid RW. J Geophys Res. 2013; doi: 10.1002/jgra.50317

Borson EN. Proc of SPIE. 2004; 5526doi: 10.1117/12.562179

e2v technologiesCCD42-80 Back Illuminated High Performance CCD Sensor E2v technologies; Mar, 2006 A1A-100025 Issue 9http://www.e2v.com/shared/content/resources/File/documents/imaging-space-and-scientific-sensors/12-42-80.pdf Accessed 05 May 2016

Ellis S. MIGHTI Stray Light Analysis Update, Photon Engineering LLC. Nov 25.2014 Report dated.

Englert CR, Harlander JM, Cardon JG, Roesler FL. Appl Opt. 2004; doi: 10.1364/AO.43.006680

Englert CR, Harlander JM. Appl Opt. 2006; 45:4583. [PubMed: 16799669]

Englert CR, Babcock DD, Harlander JM. Appl Opt. 2007; 46:7297. [PubMed: 17932544]

Englert CR, Stevens MH, Siskind DE, Harlander JM, Roesler FL. J Geophys Res. 2010a; doi: 10.1029/2010JD014398

Englert CR, Harlander JM, Emmert JT, Babcock DD, Roesler FL. Opt Ex. 2010b; 18:27416.

Englert CR, Harlander JM, Brown CM, Meriwether JW, Makela JJ, Castelaz M, Emmert JT, Drob DP, Marr KD. J Atmos Sol-Terr Phys. 2012; doi: 10.1016/j.jastp.2012.07.002

Fruit M, Gusarov A, Doyle D. SPIE Proc. 2002; 4823:132.

Gault WA, Brun JF, Desaulniers DL, Miller DW, Pasternak F, Rochon Y, Rupil JM, Shepherd GG. SPIE Proc. 1992; 1753:189.

Harding BJ, Makela JJ, Englert CR, Marr KD, Harlander JM, England SL, Immel TJ. Space Sci Rev this issue. 2017

Harlander JM, Reynolds RJ, Roesler FL. Astrophys J. 1992; 396:730.

Harlander JM, Englert CR, Babcock DD, Roesler FL. Opt Ex. 2010; 18:26430.

Harlander JM, Englert CR, Brown CM, Marr KD, Miller I, Zastera V, Immel TJ. Space Sci Rev this issue. 2017

Hays PB, Abreu VJ, Dobbs ME, Gell DA, Grassl HJ, Skinner WR. J Geophys Res. 1993; 98:10713.

Immel TJ, et al. Space Sci Rev this issue. 2017

Killeen TL, Wu Q, Solomon SC, Ortland DA, Skinner WR, Niciejewski RJ, Gell DA. J Geophys Res. 2006; doi: 10.1029/2005JA011484

Lathuillière C, Gault WA, Lamballais B, Rochon YJ, Solheim BH. Ann Geophys. 2002; 20:203.

Liu G. PhD Dissertation York University; Toronto, Ontario, Canada: 2006

Lucas RA, , et al. ACS Data Handbook Baltimore: STScI; 2016 Version 8.0

Marr KD, Englert CR, Harlander JM. Opt Ex. 2012; doi: 10.1364/OE.20.009535

Marr KD, Englert CR, Harlander JM, Miller KW. Appl Opt. 2013; doi: 10.1364/AO.52.008082

McLinden CA, McConnell JC, Griffioen E, McElroy CT. Can J Phys. 2002; doi: 10.1139/P01-156

Mende SB, Swenson GR, Llewellyn EJ, Denig WF, Kendall DJW, Slanger TG. J Geophys Res. 1988; 93:12,861.

MIGHTI Flight Model Calibration Report. SSD-RPT-MI013 Rev-. 2016

Morrow ML, Morrow WH, Majorana L. SPIE. 1993; 1945:478–483.

Noxon JF, Vallence Jones A. Nature. 1962; doi: 10.1038/196157a0

Ogilvie KW, et al. Space Science Reviews. 1995; 71:55–77.

Peterson JQ, , Cardon JG, , Sevilla P, , Hancock J, , Englert CR, , Harlander JM, , Brown CM, , Marr KD. MIGHTI Spectral Calibration. CALCON Technical Meeting; 22-25 August 2016; Logan UT.

Rees D, Fuller-Rowell TJ, Lyons A, Killeen TL, Hays PB. Appl Opt. 1982; 21:3896. [PubMed: 20396337]

Sheese PE, Llewellyn EJ, Gattinger RL, Bourassa AE, Degenstein DA, Lloyd ND, McDade IC. Can J Phys. 2010; 88:919.

Sheese PE, Llewellyn EJ, Gattinger RL, Bourassa AE, Degenstein DA, Lloyd ND, McDade IC. Geophys Res Lett. 2011; doi: 10.1029/2011GL047437

Shepherd GG, Thuillier G, Gault WA, Solheim BH, Hersom C, Alunni JM, Brun J-F, Brune S, Charlot P, Cogger LL, Desaulniers D-L, Evans WFJ, Gattinger RL, Girod F, Harvie D, Hum RH, Kendall DJW, Llewellyn EJ, Lowe RP, Ohrt J, Pasternak F, Peillet O, Powell I, Rochon Y, Ward WE, Wiens RH, Wimperis J. J Geophys Res. 1993; doi: 10.1029/93JD00227

Shepherd GG, Thuillier G, Cho YM, Duboin ML, Evans WFJ, Gault WA, Hersom C, Kendall DJW, Lathuillère C, Lowe RP, McDade IC, Rochon YJ, Shepherd MG, Solheim BH, Wang DY, Ward WE. Rev Geophys. 2012; doi: 10.1029/2012RG000390

Smith WJ. Modern Optical Engineering 2nd. New York: McGraw-Hill; 1990139ff

Stevens MH, Englert CR, Harlander JM, England SL, Marr KD, Brown CM, Immel TJ. Space Sci Rev. 2017 this issue.

Thuillier G, Gault W, Brun JF, Hersé M, Ward W, Hersom C. Appl Opt. 1998; 37:1356. [PubMed: 18268723]

Wallace L, Hunten DM. J Geophys Res. 1968; 15:4813.

Wu DL, Schwartz MJ, Waters JW, Limpasuvan V, Wu Q, Killeen TL. Adv Space Res. 2007; doi: 10.1016/j.asr.2007.06.014

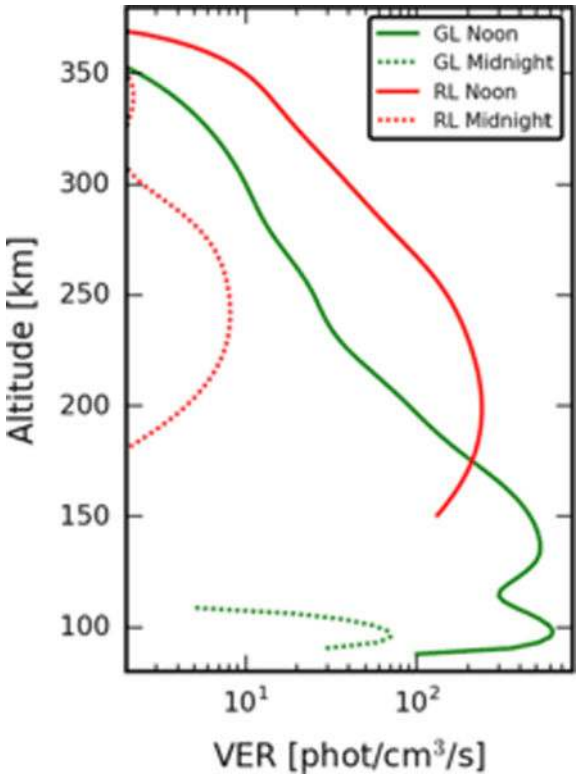

Figure 1.
Volume emission rates of the oxygen green (GL) and red (RL) line emissions used for the MIGHTI instrument model.

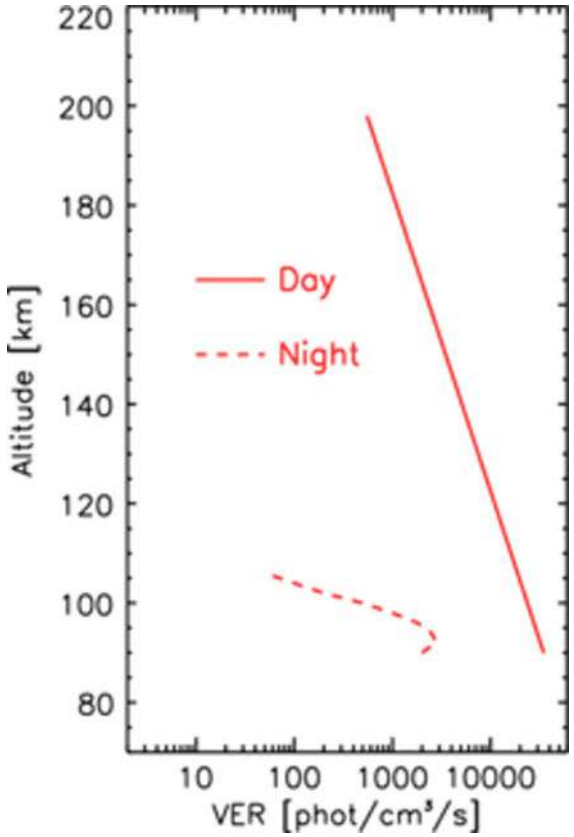

Figure 2.
Average volume emission rates of the oxygen A-band used for the MIGHTI instrument model.

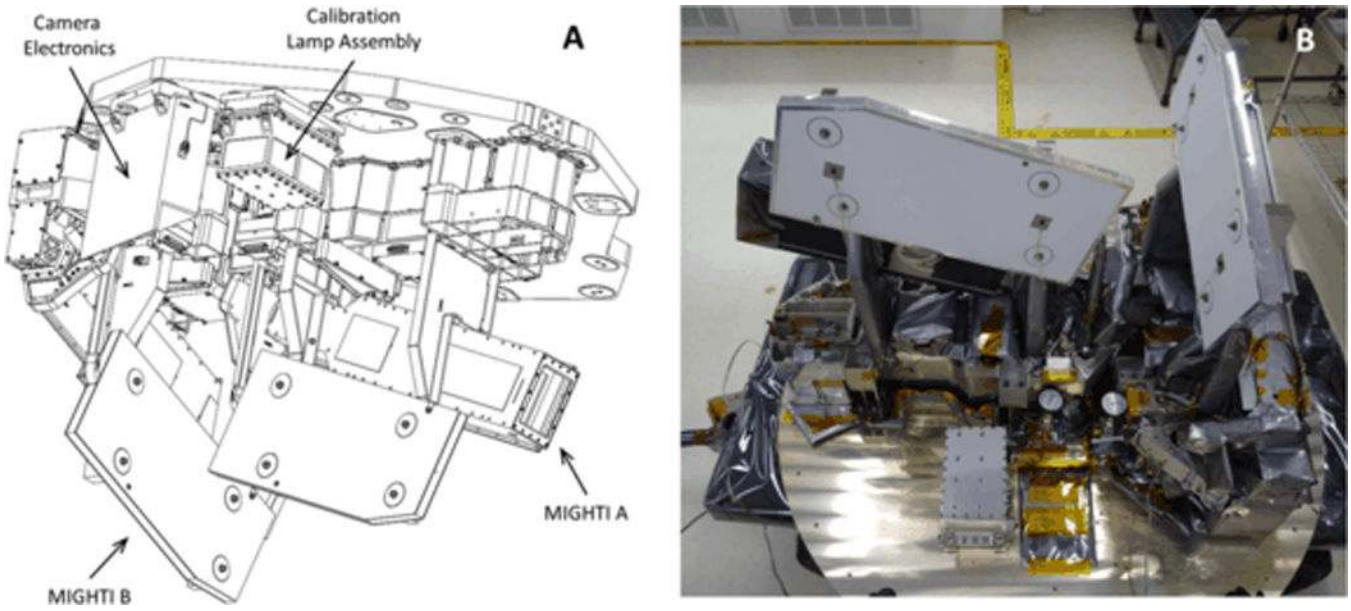

Figure 3.

(A) Isometric view of the MIGHTI instrument integrated on the ICON Payload Interface Plate (PIP). In this view the zenith direction is up and the MIGHTI sensors are pointed downward at the Earth's limb. (B) MIGHTI optical sensors and the calibration lamp assembly prior to the integration on the PIP.

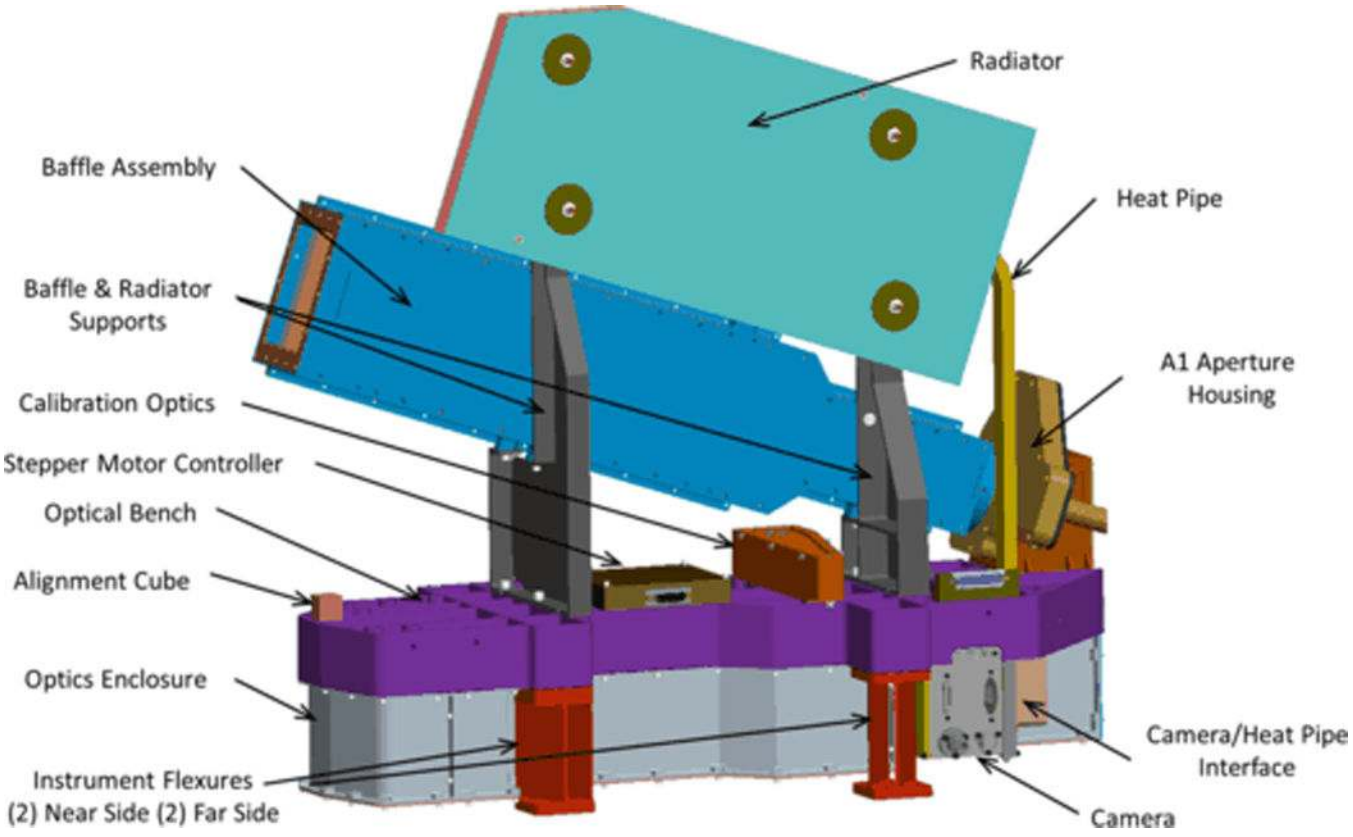

Figure 4.
A single MIGHTI sensor unit.

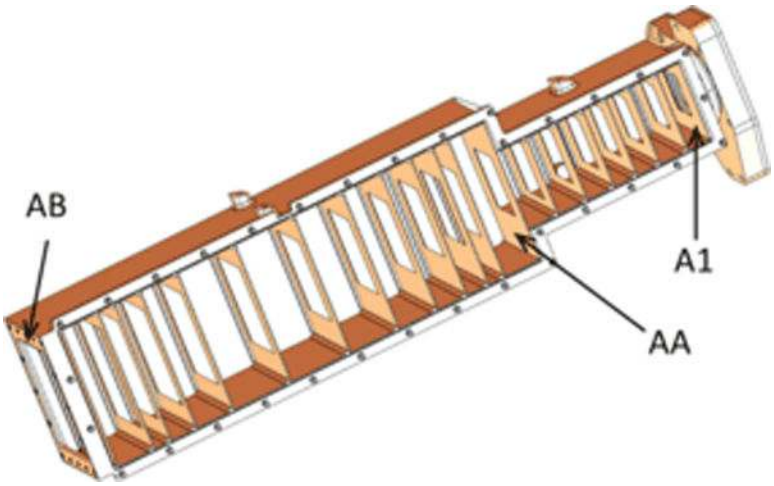

Figure 5.

MIGHTI baffle with the sidewall removed. On the top right, the mechanism housing for the day/night aperture, A1, at the pupil is shown. The inside surfaces of the baffles are coated with black epoxy primer (Cytec Industries BR 127NC).

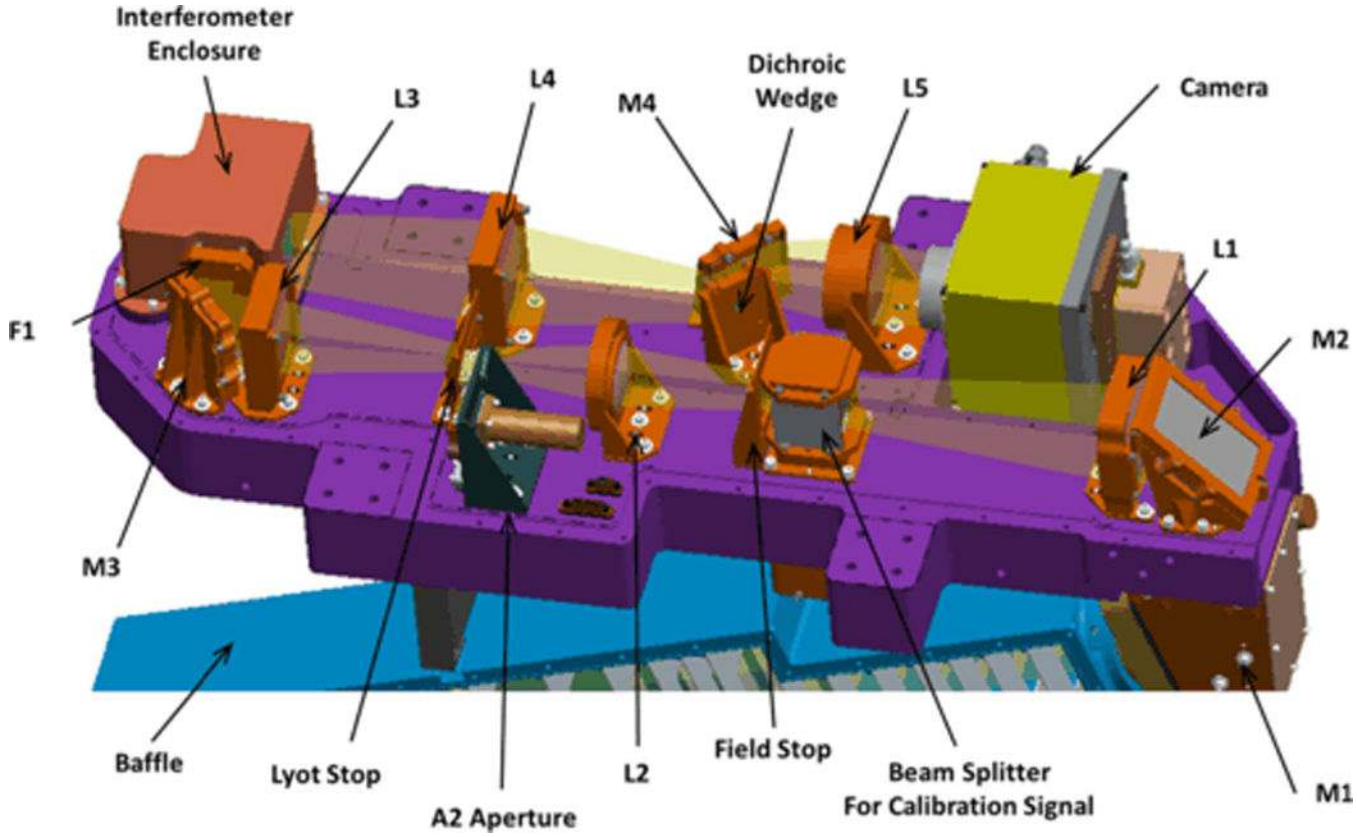

Figure 6.
MIGHTI optical bench (purple) populated with all optical elements. L denotes lenses, M denotes mirrors, F denotes interference filters.

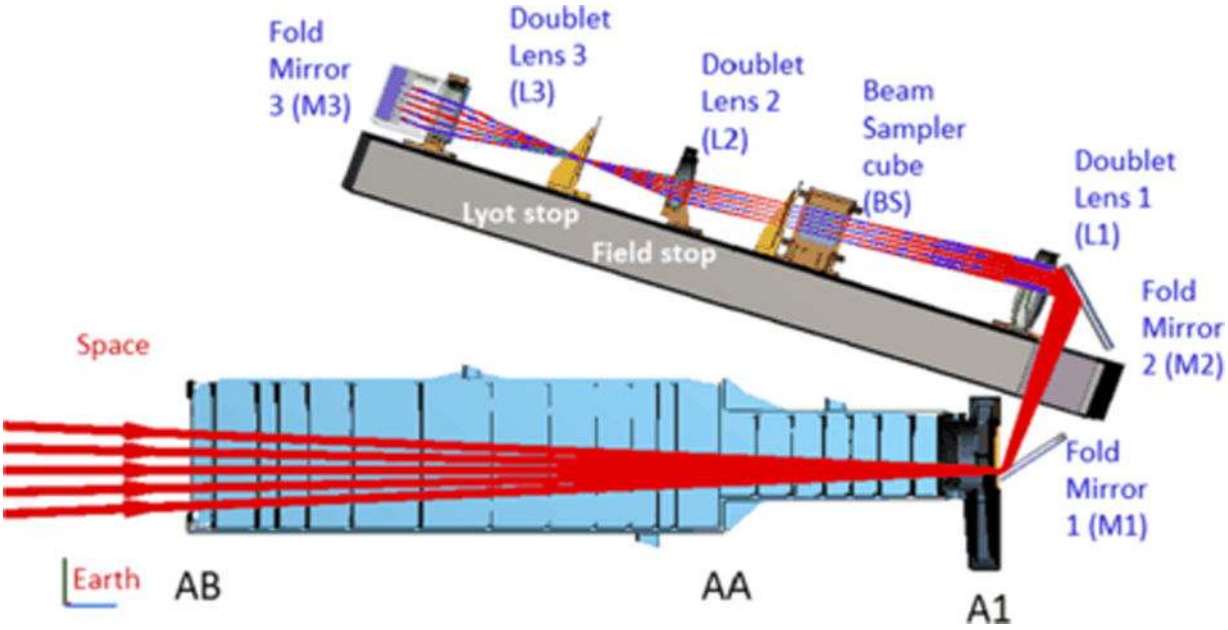

Figure 7.
Geometry of MIGHTI baffle stray light model. Rays shown are for the A1 15% position.

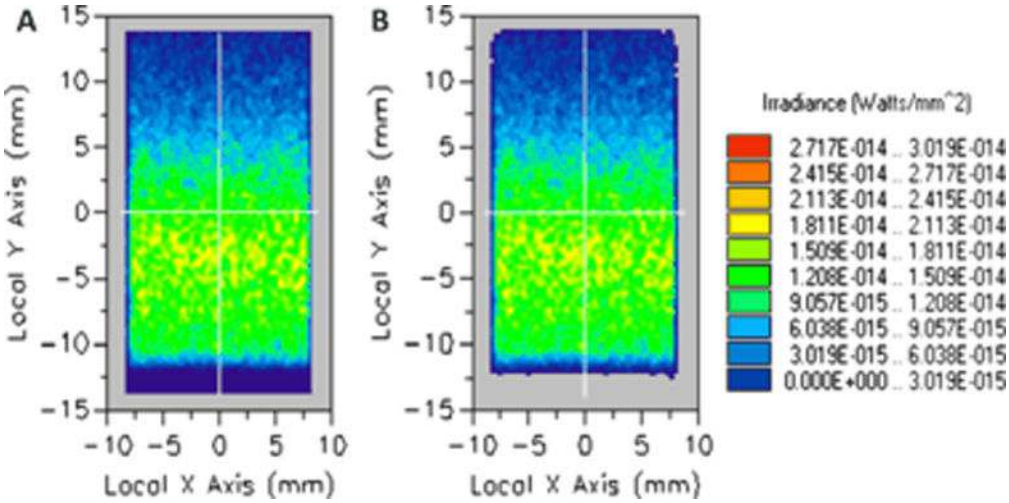

Figure 8.

Results for scattered light calculation from the illuminated Earth's disk at 630nm. The images show the flux at the interferometer gratings. (A) All rays; (B) direct rays only, no ghosts, no scatter. Integrated flux: All rays: 4.490×10^{-12}W; Direct rays: 4.436×10^{-12}W. Ghosts plus scatter amount to 5.4×10^{-14}W or 1.2% of the direct signal

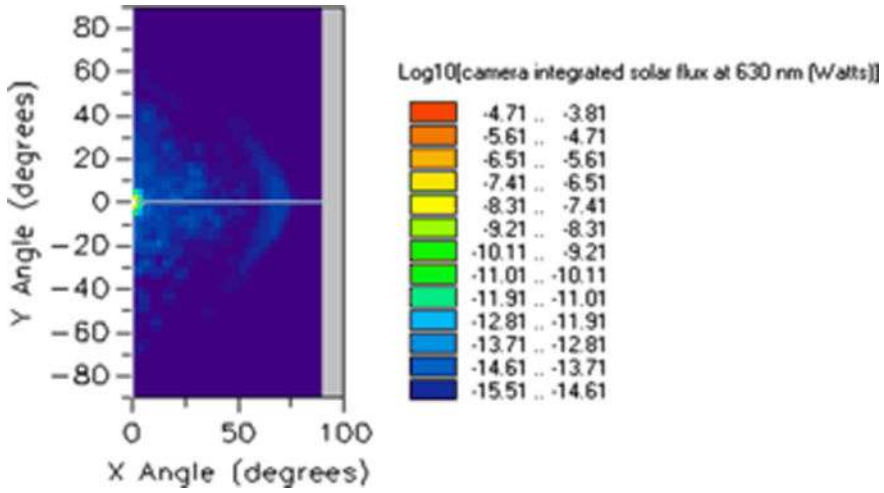

Figure 9.

Integrated solar flux at MIGHTI image plane at λ=630nm within a 2nm passband. The integrated solar flux drops below the 10% threshold at angles greater than 6°.

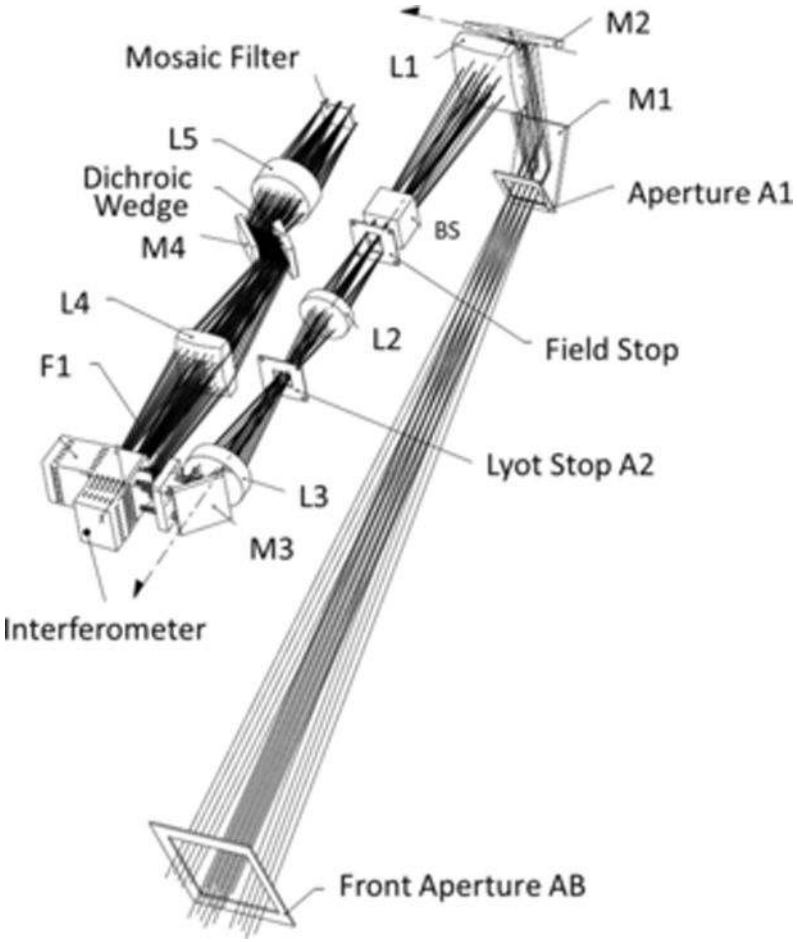

Figure 10.
MIGHTI optical components shown with representative rays.

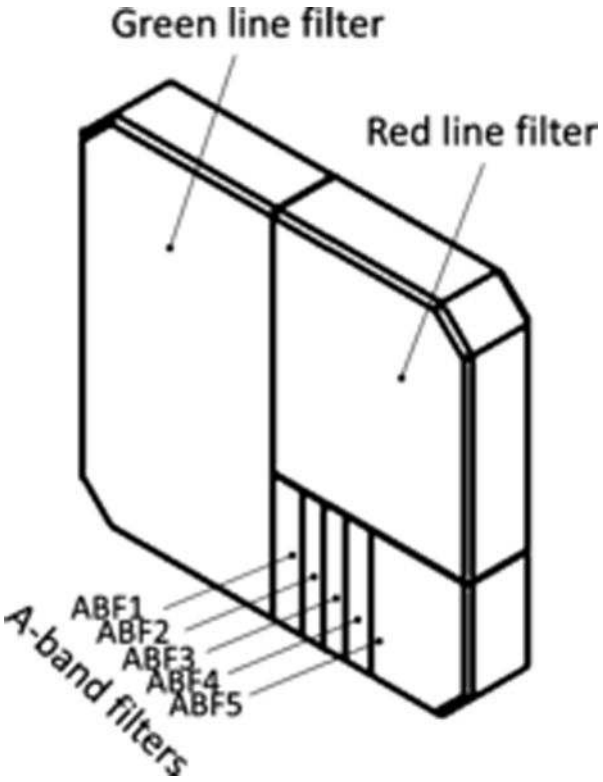

Figure 11.
Mosaic filter geometry.

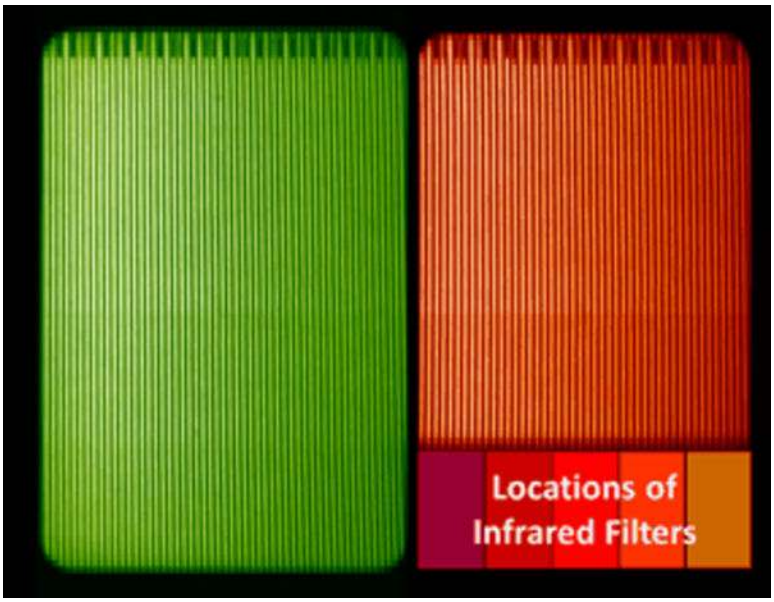

Figure 12.

False color image of calibration lamp signal taken with MIGHTI A. This image is binned by 2 pixels in the vertical and 2 pixels in the horizontal dimension. On orbit, the binning will be 16 × 2 (vertical × horizontal) and the vertical dimension will cover the tangent point altitudes between about 90-300km. The top of both red and green images show the periodic notch pattern that is inscribed onto one of the gratings of each interferometer. This pattern is used to track any residual horizontal image shifts on the CCD detector [Englert et al. 2010b]. The locations of the NIR filters are shown on the bottom right using superimposed rectangles as they are not illuminated by the calibration lamps.

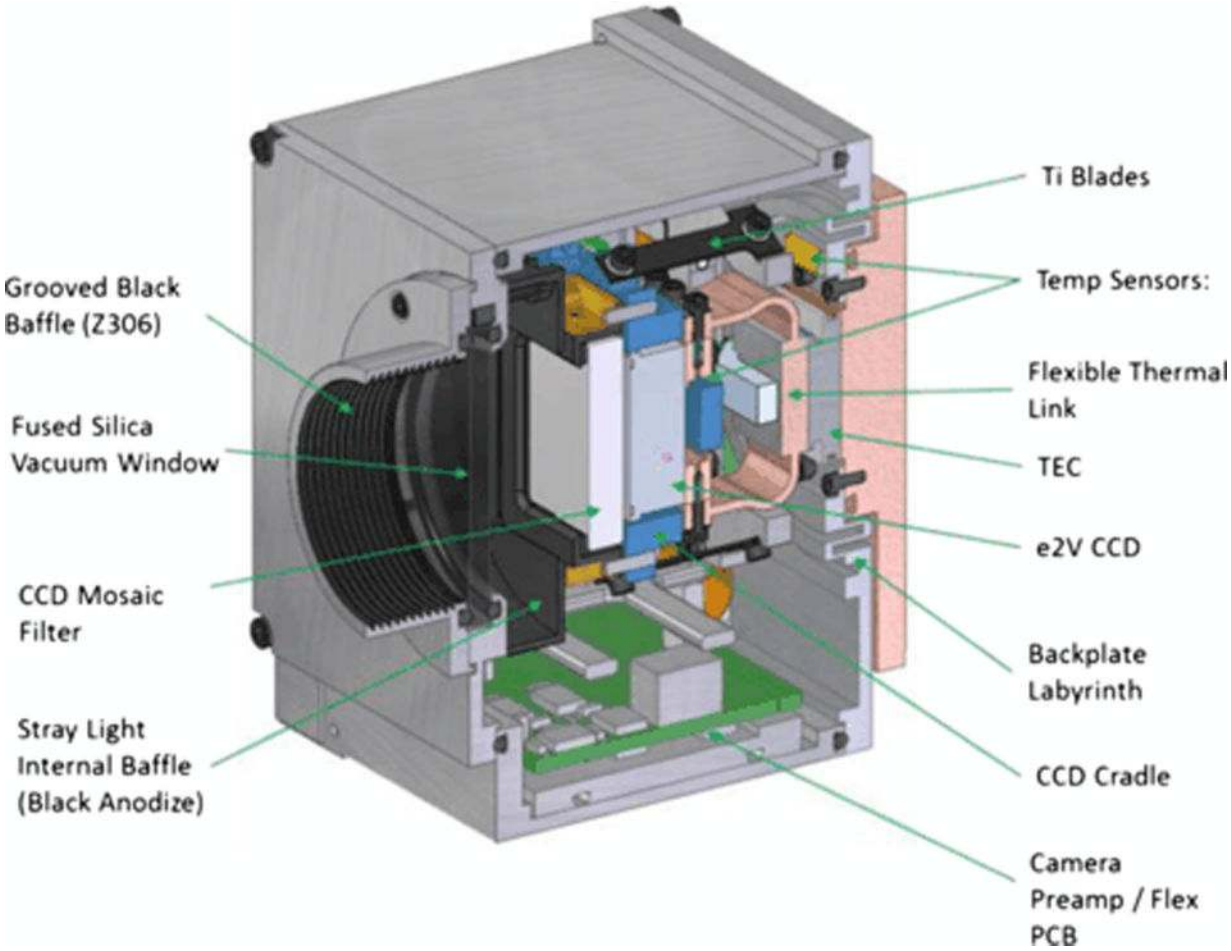

Figure 13.
MIGHTI camera head cut-away.

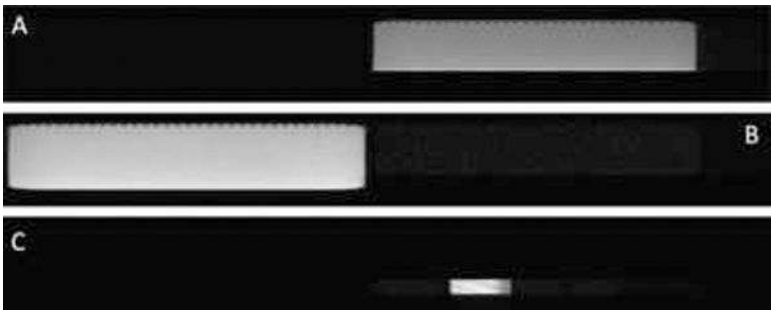

Figure 14.

Example responsivity images at specific wavelengths taken with MIGHTI A in day mode (1026×128 binned pixels, 16×2 binning). (A) λ =630.03nm; (B) λ =557.71nm; and (C) λ =759.99nm. The grayscale covers the dynamic range from zero (black) to the maximum signal in each panel (white). Note that the responsivities for the oxygen red and green lines do not have significant small scale structure, except for the notches at the top. The slowly changing variations are most likely dominated by variations in the mosaic filter. The NIR channels show small scale structure, most likely due to fringing within the CCD. Using these spectral responsivity measurements this structure can be accounted for in data analysis.

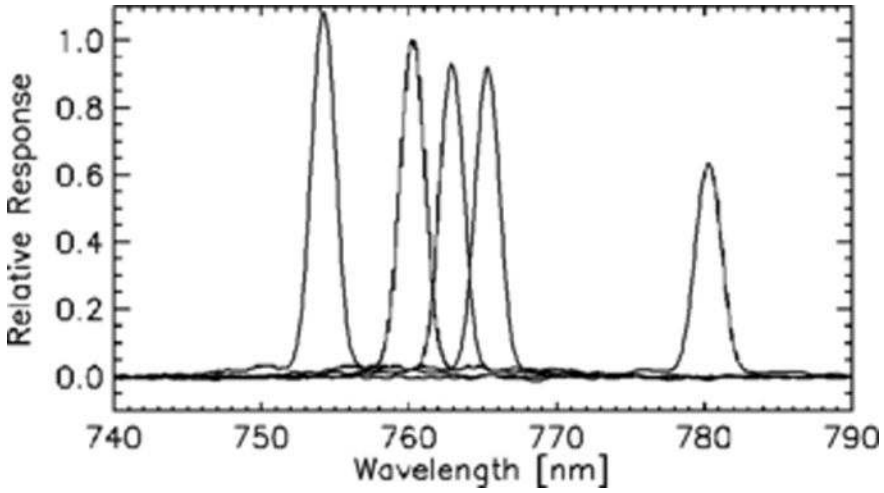

Figure 15.

Spectral response within the areas of all five NIR filters. Each curve represents an average spectral response of 36 binned pixels in one CCD row at approximately the center altitude covered by the filters. The response shape is dominated by the passband of the narrow band filters. The three passbands in the middle are within the oxygen A-band, the remaining two are used to perform a background signal subtraction [Stevens et al. 2016].

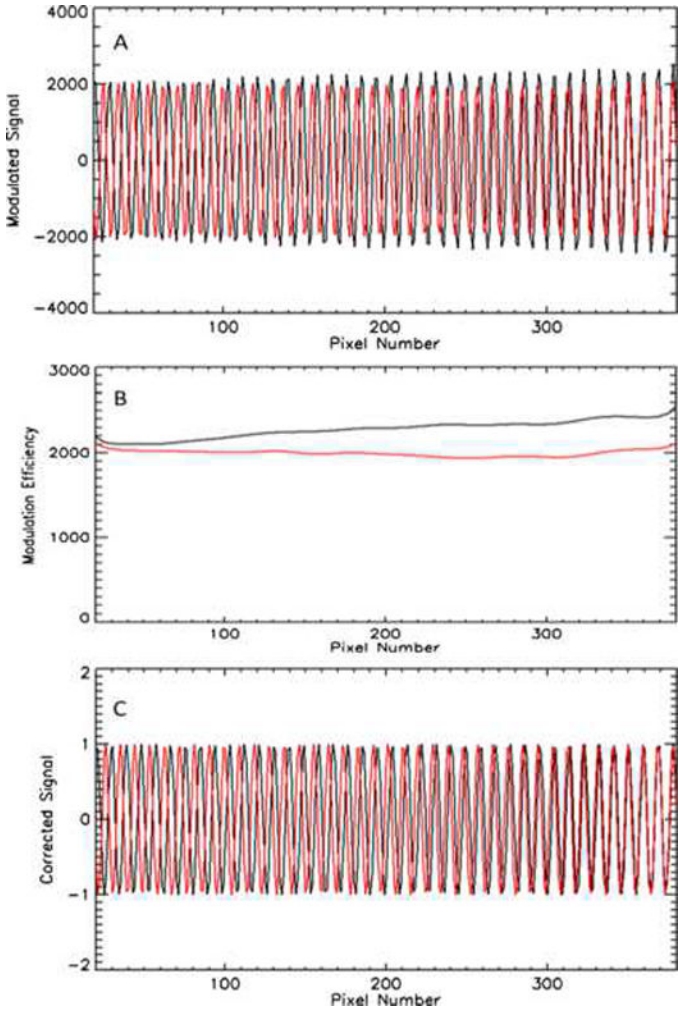

Figure 16.

(A) Modulated part of a responsivity- and dark-corrected interferogram measured using the external integrating sphere illuminated with a neon lamp. Two binned pixel CCD rows near the top and the bottom of the altitude range are shown for MIGHTI A in night mode to illustrate row to row differences in the modulation efficiency. Signal is in arbitrary units. (B) Calculated modulation efficiency for the two rows in (A). (C) Modulation efficiency corrected fringe patterns for the two rows shown in (A). Note that the fringe amplitude after the correction is now constant (normalized) and equal for both.

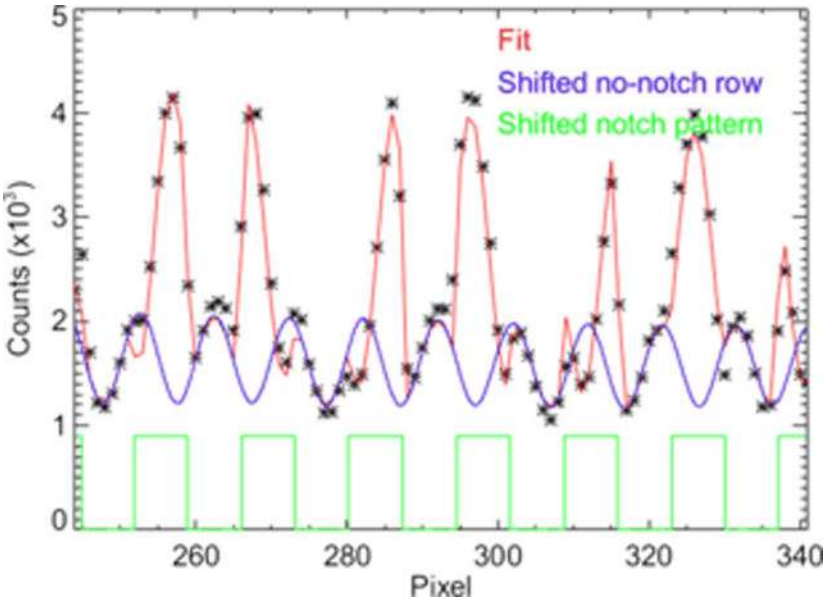

Figure 17.

Locating the horizontal notch pattern position. The stars indicate the measured values (Ne calibration lamp) for a pixel row containing the notch pattern. The blue curve indicates a scaled and phase shifted fringe pattern from a pixel row just below the notch pattern to optimally fit the pixels that fall inside the notches. For the pixels that fall outside the notches, an analogous fringe pattern is obtained by scaling and phase shifting the same fringe pattern from below the notches (not shown for clarity). The red curve indicates the final least squares fit result that contains the scaled and phase shifted values for the pixels that are either fully in or fully outside the notches. The values for the pixels that contain a notch boundary are calculated using contributions from both on a subpixel level, e.g., 435/1000th signal from within the notch and 565/1000th signal from outside the notch. The resulting best fit notch pattern position is shown in green where 0.0 and 0.9 correspond to inside and outside of the notches respectively.

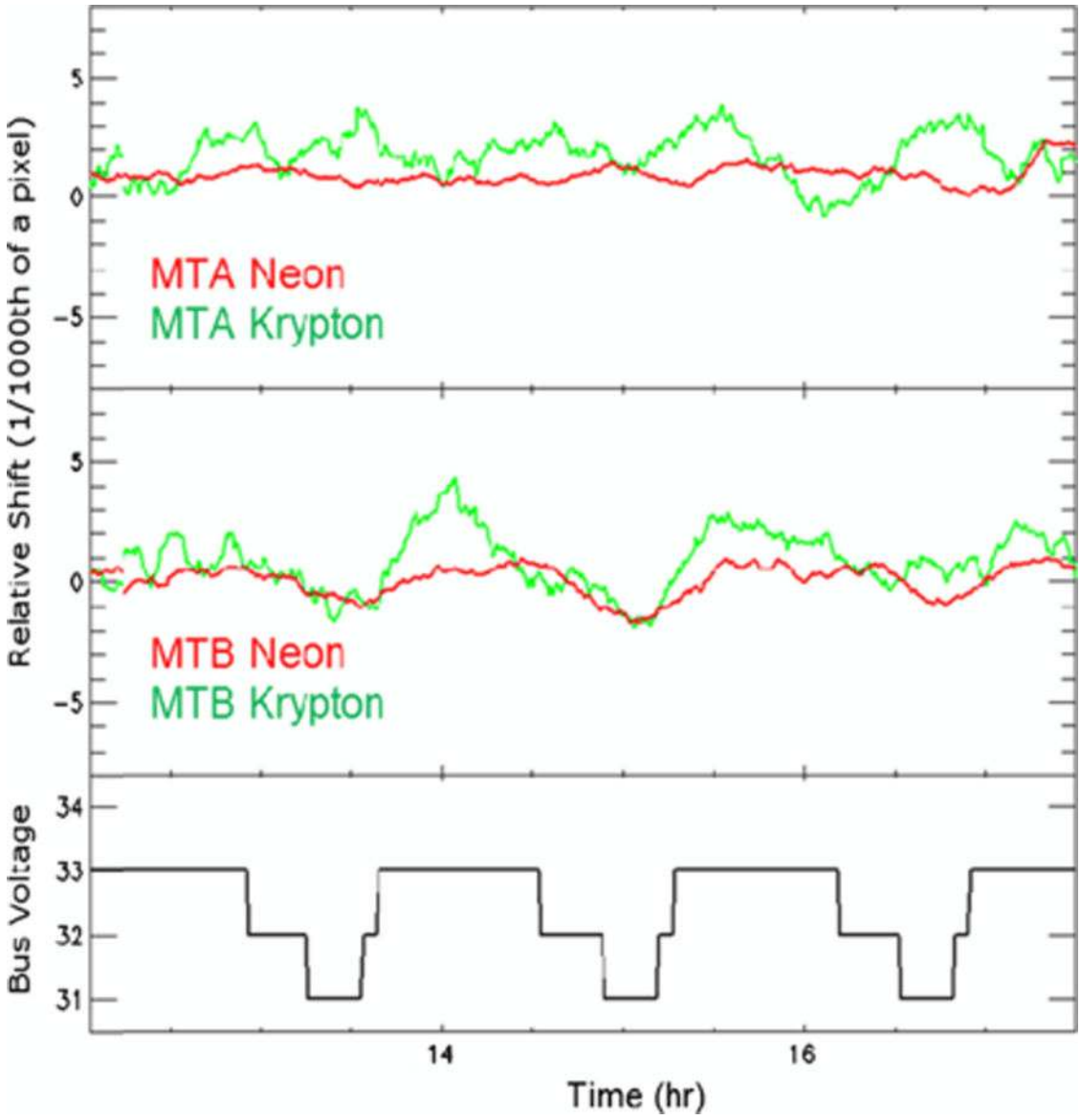

Figure 18.

Fringe image shift derived from the locations of the grating notches during the simulation of the anticipated on-orbit thermal changes, driven by the changing bus voltage.

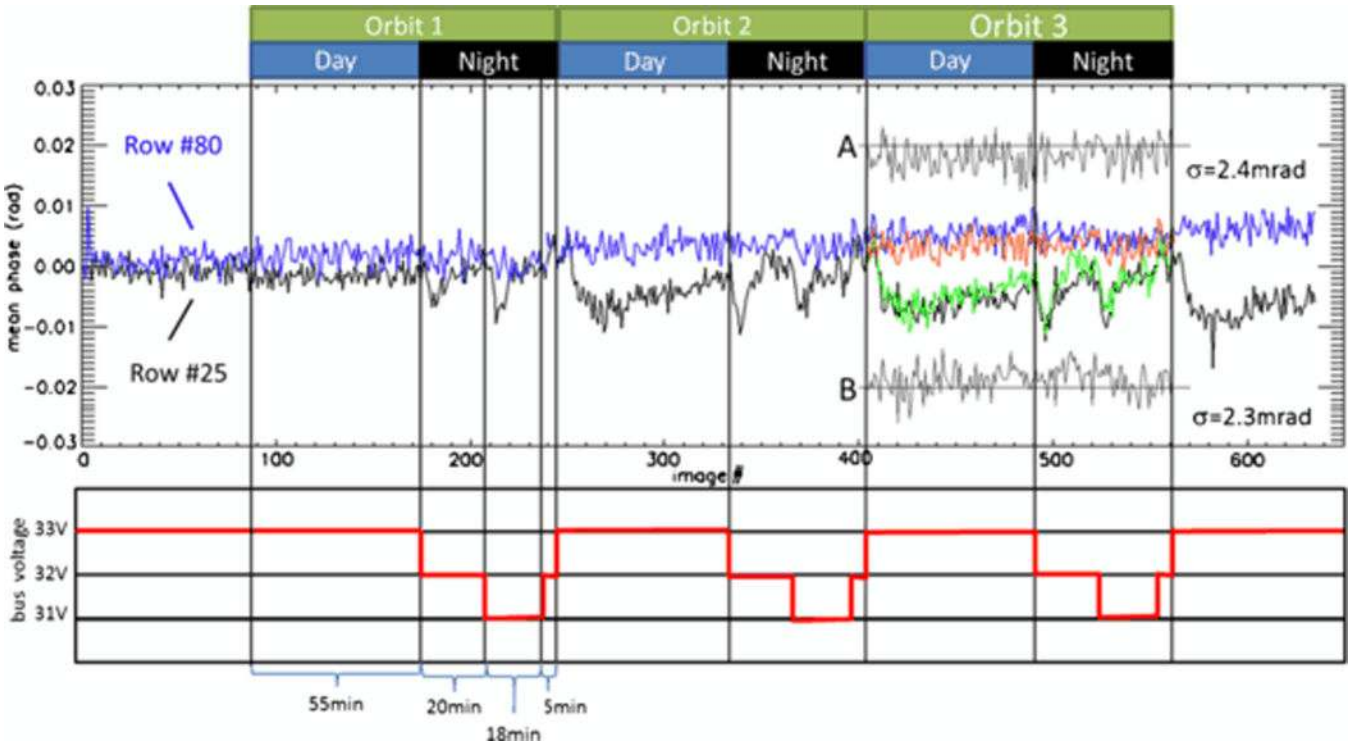

Figure 19.

Top panel: Black, blue: Mean fringe phase versus image number for two rows (25 and 80, respectively), which correspond to tangent altitudes of approximately 300km and 150km (top and bottom of red fringes, MIGHTI B, red-line). Red, green: Phase data from simulated Orbit 2 shifted to line up with Orbit 3 for comparison. A, B: Difference of red-blue and green-black, shifted up and down for clarity. Horizontal lines show zero difference. Bottom panel: Corresponding bus voltage versus image number. Integration time was 30s, interval between images was about 7.6 sec (Ground support equipment (GSE) read out time). No dark, flatfield, or spike correction was performed for this analysis.

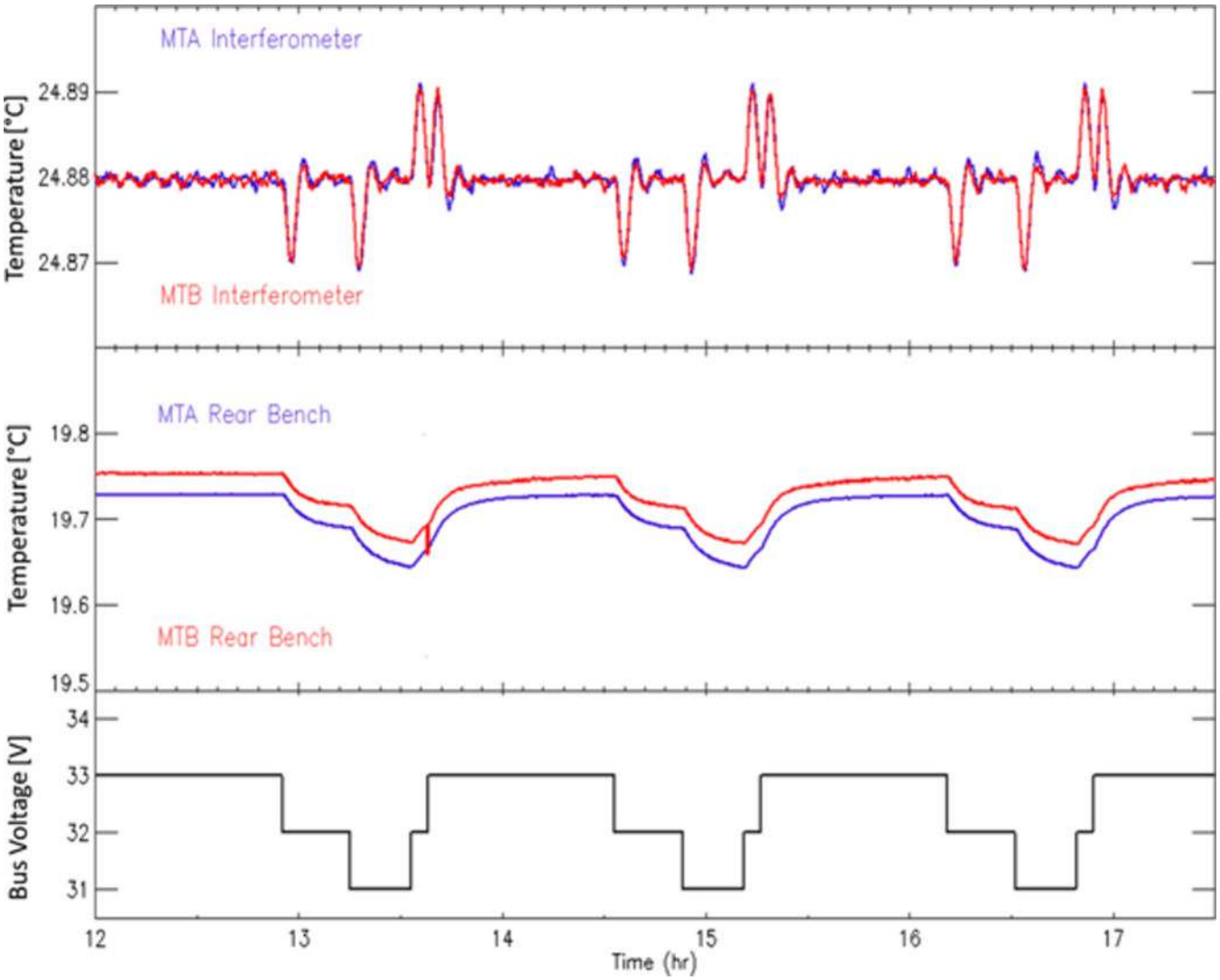

Figure 20.

Sensor baseplate (rear optical bench, close to the CCD detectors) and interferometer temperatures, as measured during the orbit simulation for which the bus voltage was changed to simulate orbit day/ night transitions.

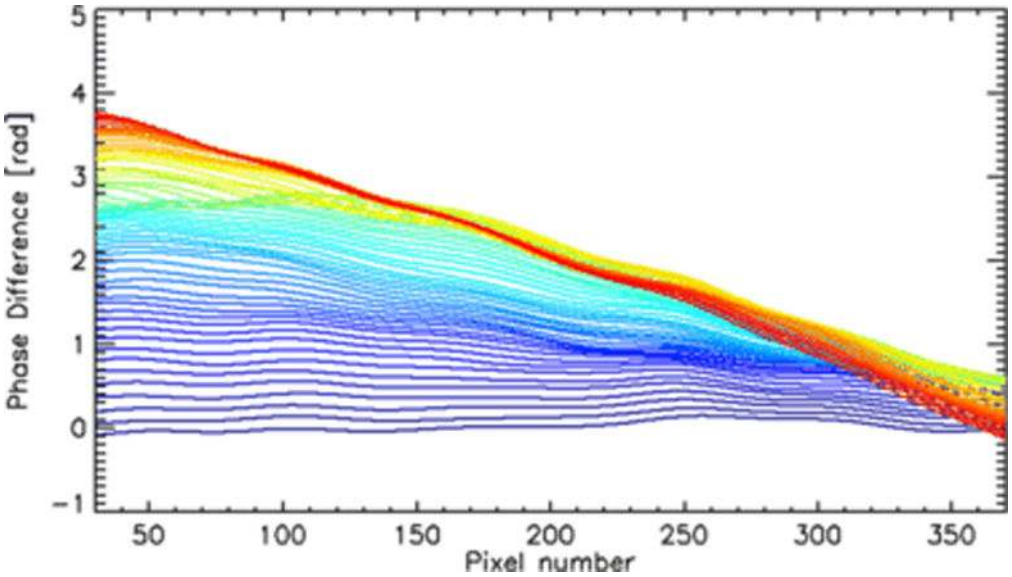

Figure 21.

Phase distortion for 57 16 × 2 binned rows (25 to 81) corresponding to tangent point altitudes ~150-300km. The colors from red to blue are for increasing altitude. The data for this analysis is from MIGHTI A using the night mode and an external neon source illuminating the FOV via an integrating sphere.

Table 1

MIGHTI single field of view wind speed measurement requirements for altitude dependent wind components in the line of sight direction

Altitude Range [km]	Day	Night	Vertical Resolution [km]	Along Track Resolution [km]	Wind Velocity Precision [m/s]
90-105	x	x	5	500	8.7
105-170	x		5	500	10
170-200	x		30	500	10
200-300	x	x	30	500	8.7

Space Sci Rev. Author manuscript; available in PMC 2018 October 01.

Table 2

MIGHTI single line of sight temperature measurement requirements.

Altitude Range [km]	Day	Night	Vertical Resolution [km]	Along Track Resolution [km]	Temperature Precision [K]
90-105	x	x	5	500	12

Table 3

Minimum instrument requirements, design values, and as-built performance.

Instrument Parameter	Requirement/Design Value	As-built value (MIGHTI A & B)
Field of View (vert × horiz)	5.36° × 3.22°	> 5.36° × 3.22°
Total Etendue (AΩ) for 85-310km limb scene (top 8km are used for thermal tracking)	0.0495 cm^2 sr (Night) 0.0074 cm^2 sr (Day)	> 0.0495 cm^2 sr (Night) > 0.0074 cm^2 sr (Day)
Interferometer Optical Path ± Difference Interval	5.1±0.4cm	Red: 4.89±0.4cm (A), 4.94±0.4cm (B) Grn: 4.85±0.4cm (A), 4.90±0.4cm (B)
Interferometer Echelle Grating Groove Density	64 grooves/mm	64.285 grooves/mm
Monochromatic Interferometer Fringe Contrast	Red Day: 66% Red Night: 57% Green Day: 43% Green Night: 43%	Red Day: 78% (A), 78% (B) Red Night: 73% (A), 72% (B) Green Day: 78% (A), 85% (B) Green Night: 75% (A), 83% (B)
Optical Efficiency (EOL) (incl. all optics, filters and CCD quantum efficiency)	Red: 15.8% Green: 11.5%	Red: 18.7% Green: 14.7%
CCD Dark Current @ −40° C (EOL)	0.1 elec./sec./pix	0.02 elec./sec./pix
CCD Read Out Noise	16.8 (rms) e/binned pixel/read	<4.2 (rms) e/binned pixel/read
Stray Light Amount (day only)	35% of max. red line signal	<10% (by analysis)

The requirements are based on a 2k×2k CCD array and 16×2 (vertical × horizontal) pixel binning (see Section 3). EOL stands for end-of-life, CCD for charge-coupled device. The as-built interferometer fringe contrast specifications include the modulation transfer function effect of the exit optics and the small contrast reduction resulting from the finite width of the binned detector pixels. The optical efficiency is derived from the measured component performances. The EOL dark current is assumed to be a factor of two higher than the measured pre-launch value [Lucas et al. 2016].

Table 4

Median filter passband center wavelengths (CWL) and spectral widths (full width half maximum) as measured at the CCD pixels with the day and night aperture positions for MIGHTI A. The values for day and night are different because of the different illumination of the filter. The data for MIGHTI B filters is similar.

	Red	Green line filter	A-band Filter 1	A-band Filter 2	A-band Filter 3	A-band Filter 4	A-band Filter 5
CWL day [nm]	630.17	557.99	754.22	760.23	762.87	765.28	780.29
Width day [nm]	1.97	1.91	1.92	1.95	1.92	1.93	2.07
CWL night [nm]	630.31	558.02	754.51	760.54	763.17	765.57	780.59
Width night [nm]	1.99	1.90	2.05	2.09	2.05	2.06	2.18

Table 5

As-built MIGHTI camera performance

Camera Parameter	Parameter Value
Dark current @ −40°C [electrons/pixel/s]	0.01 (beginning of life)
Read out noise [RMS electrons]	<4.2 (for gain of ~1.65 electrons/digital number)
Gain [electrons/digital number]	~1.65 (two more gains available via command)
Power consumption [W]	11.0 to 12.9 depending on mode and bus voltage
Frame transfer time [ms]	307.5
On chip pixel binning	commandable (on-orbit: 1×1 or 16×2)

Table 6

Level 0 to Level 1 data analysis steps

Calibration Steps for Wind Observations	Calibration Steps for Temperature Observations
Dark current and bias correction	Dark current and bias correction
Spike removal	Spike removal
Pixel transfer pick-up correction	Pixel transfer pick-up correction
Flatfield correction	Horizontal binning
Fringe modulation efficiency correction	
Phase correction for thermal image shift	
Phase distortion correction	
Phase correction for interferometer thermal drift	

Table 7

Center path difference.

	MIGHTI A	MIGHTI B
Red-line	4.89 ± 0.12cm	4.85 ± 0.16cm
CCD Column Number (Red)	314	315
Green-line	4.94 ± 0.12cm	4.90 ± 0.16cm
CCD Column Number (Green)	777	774

Table 8

Path difference change per binned pixel.

	MIGHTI A	MIGHTI B
Red-line Path Difference per Binned Pixel	23.997μm	23.997μm
Green-line Path Difference per Binned Pixel	21.115μm	21.264μm